Gondwana Research 94 (2021) 222–242

Contents lists available at ScienceDirect

Gondwana Research

journal homepage: www.elsevier.com/locate/gr

Late Paleozoic Gondwanide deformation in the Central Andes: Insights from RSCM thermometry and thermal modeling, southern Bolivia

Ryan B. Anderson [a,*,1], Sean P. Long [a], Brian K. Horton [b,c], Amanda Z. Calle [b,2], Emmanuel Soignard [d]

[a] School of the Environment, Washington State University, USA
[b] Department of Geological Sciences, Jackson School of Geosciences, University of Texas at Austin, USA
[c] Institute for Geophysics, Jackson School of Geosciences, University of Texas at Austin, USA
[d] Eyring Materials Center, Arizona State University, USA

ARTICLE INFO

Article history:
Received 23 June 2020
Received in revised form 18 December 2020
Accepted 2 March 2021
Available online 14 March 2021

Handling Editor: T. Gerya

Keywords:
Raman spectroscopy of carbonaceous material thermometry
Gondwanide orogeny
Western Gondwana
Pre-Andean tectonics
Bolivia

ABSTRACT

A widespread unconformity between Ordovician metasedimentary rocks and nonmetamorphosed Mesozoic sedimentary rocks across the Eastern Cordillera of Bolivia provides evidence for significant pre-Late Cretaceous deformation and erosion. In this paper, we refine the middle to late Paleozoic tectonic history of the central Andean segment of Gondwana's western margin. We combine Raman spectroscopy of carbonaceous material (RSCM) thermometry with semi-quantitative deformation temperature estimates from quartz recrystallization microstructures and published illite crystallinity values from Cambrian-Devonian sedimentary rocks that span the Eastern Cordillera of southern Bolivia at ~21°S. Estimates of peak temperature and deformation temperature range primarily between ~220 and ~ 400 °C and show a general increase with depth that defines a metamorphic field gradient between ~37 and ~ 47 °C/km. Temperatures obtained from Ordovician rocks directly below the unconformity require erosion of a > ~5 km overburden prior to the Late Cretaceous, which was likely accomplished by a combination of distributed cleavage development and Paleozoic folding and thrust faulting revealed from cross-section reconstructions. The peak temperature data are incorporated into thermal models along with published illite K—Ar, zircon (U—Th)/He, and zircon fission-track cooling ages that refine the timing of Paleozoic orogenesis in the central Andes. We interpret shortening-related flexural subsidence driven by cratonward growth of a pre-Andean orogenic wedge along the western margin of Gondwana, with peak temperature conditions attained during eastward advance of a foreland basin between ~420 and ~ 318 Ma during the Devonian-Carboniferous Gondwanide Orogeny. Erosional exhumation between ~352 and ~ 294 Ma was the result of continued growth and eastward expansion of the associated Transpampean tectonic highland across the Eastern Cordillera. The growth of this pre-Andean contractional orogen coincided with global plate reorganization and the reestablishment of subduction and arc magmatism along the western margin of Gondwana, as indicated by a significant influx of Carboniferous arc-related detritus into the foreland basin system.

© 2021 International Association for Gondwana Research. Published by Elsevier B.V. All rights reserved.

1. Introduction

Documenting the architecture, kinematics, and thermal history of ancient mountain belts is critical for understanding the processes of basin development, the controls that inherited structures and basin architecture can exert on later orogenesis, and how successive orogenic events can influence the distribution and quality of petroleum systems (e.g., Allmendinger et al., 1983; Mpodozis and Ramos, 1989; Kley et al., 1999; DeCelles and Mitra, 1995; Pearson et al., 2012; McGroder et al., 2015). Additionally, characterizing the thermal conditions and exhumation history of ancient orogenic events can be important for understanding sediment provenance and providing context for the interpretation of cooling ages in active mountain belts (e.g., Bernet and Spiegel, 2004; Carrapa et al., 2009).

Rocks that comprised the western margin of Gondwana (Fig. 1), which are today exposed in the central Andes, were subjected to several orogenic events between the Neoproterozoic and late Paleozoic (Bahlburg and Hervé, 1997; Cawood, 2005; Ramos, 2008, 2009; McGroder et al., 2015; Heredia et al., 2018). Studies of such pre-Andean deformation, structural fabrics, and basin architecture recorded in Paleozoic rocks of northwestern Argentina and southern Bolivia have provided important context for understanding the influence of earlier orogenesis on the geometry, kinematics, and deformation history of the Cenozoic Andean fold-thrust belt and associated foreland basin

* Corresponding author at: School of the Environment, Washington State University
E-mail address: ryananderson@isu.edu (R.B. Anderson).
[1] At present: Department of Geosciences, Idaho State University, USA.
[2] At present: Bureau of Economic Geology, Jackson School of Geosciences, The University of Texas at Austin, USA.

https://doi.org/10.1016/j.gr.2021.03.002
1342-937X/© 2021 International Association for Gondwana Research. Published by Elsevier B.V. All rights reserved.

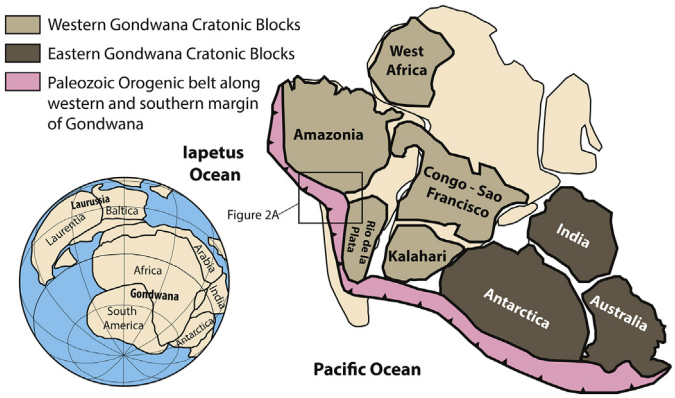

Fig. 1. Paleogeography of Gondwana, South America, and the Paleozoic orogenic belt along the margin of Gondwana in the early Carboniferous (Modified from Cawood, 2005, and Arenas and Sanchez Martinez, 2015).

(e.g., Kley, 1996; Kley et al., 1999; Mon and Salfity, 1995; Giraudo and Limachi, 2001; Carrapa et al., 2009; Giambiagi et al., 2011; Pearson et al., 2012; Anderson et al., 2017, 2018; Horton, 2018a, 2018b). At ~21°S, significant across-strike changes in the thickness and mechanical strength of pre-Cretaceous sedimentary rocks can be correlated with major changes in the structural style of Cenozoic thrust belt development (e.g., Kley, 1996; Giraudo and Limachi, 2001; Müller et al., 2002; Anderson et al., 2017). Additionally, the pre-Andean history of deformation and sedimentation played a key role in the development of hydrocarbon systems along the eastern flank of the Andes (e.g., Gohrbandt, 1993; McGroder et al., 2015). Oil and gas are produced primarily from Paleozoic epicontinental sedimentary rocks in Argentina, Bolivia, Peru, and Brazil, and their deposition was controlled by growth and erosion of a proto-Cordillera along the western Gondwanan margin (Gohrbandt, 1993). In Bolivia, the Upper Devonian Los Monos Formation and sandstones in the Lower Carboniferous section are the primary hydrocarbon source and reservoir rocks, respectively (Dunn et al., 1995); understanding their origin is critically important for characterizing the hydrocarbon resources in this region. However, unraveling the Paleozoic history of southern Bolivia has proven difficult because unclear field relationships have led to conflicting interpretations of pre-Cretaceous deformation and metamorphism (e.g., Kley and Reinhardt, 1994; Kley et al., 1997; Sempere, 1995; Starck, 1995; Jacobshagen et al., 2002; Ramos, 2008; McGroder et al., 2015), and the complex overprint of Andean deformation has obscured older structural features (e.g., Kley, 1996; Müller et al., 2002; Anderson et al., 2017).

Significant pre-Andean deformation, uplift, and erosion in the Eastern Cordillera of southern Bolivia (Fig. 2) is evident from a widespread angular unconformity between low-grade Ordovician metasedimentary rocks and nonmetamorphosed Upper Cretaceous sedimentary rocks (Sempere, 1995; Kley et al., 1997; Jacobshagen et al., 2002; Müller et al., 2002). Part of the difficulty in determining the timing of pre-Andean deformation is that development of this unconformity has been attributed to either the Ordovician Ocloyic orogeny or a separate orogenic event in the late Paleozoic (Starck, 1995; Tankard et al., 1995; McGroder et al., 2015). Also, subsequent erosion of Cenozoic *syn*-Andean sedimentary rocks across the Eastern Cordillera has made it difficult to identify pre-Andean structures (Kley et al., 1997; Müller et al., 2002). Adding to the confusion is the variable usage of the names Chañic orogeny, Hercynian orogeny, or Gondwanide orogeny to describe any late Paleozoic deformation in southern Bolivia (e.g., Starck, 1995; Tankard et al., 1995; Kley et al., 1997; Müller et al., 2002; Jacobshagen et al., 2002; McGroder et al., 2015; Ramos, 2018; Heredia et al., 2018).

Defining the thermal conditions of Paleozoic rocks in Bolivia is also challenging because few techniques are available to quantify temperatures for sub-garnet grade pelitic rocks (e.g., Long and Soignard, 2016). Accordingly, the only available temperature estimates of these

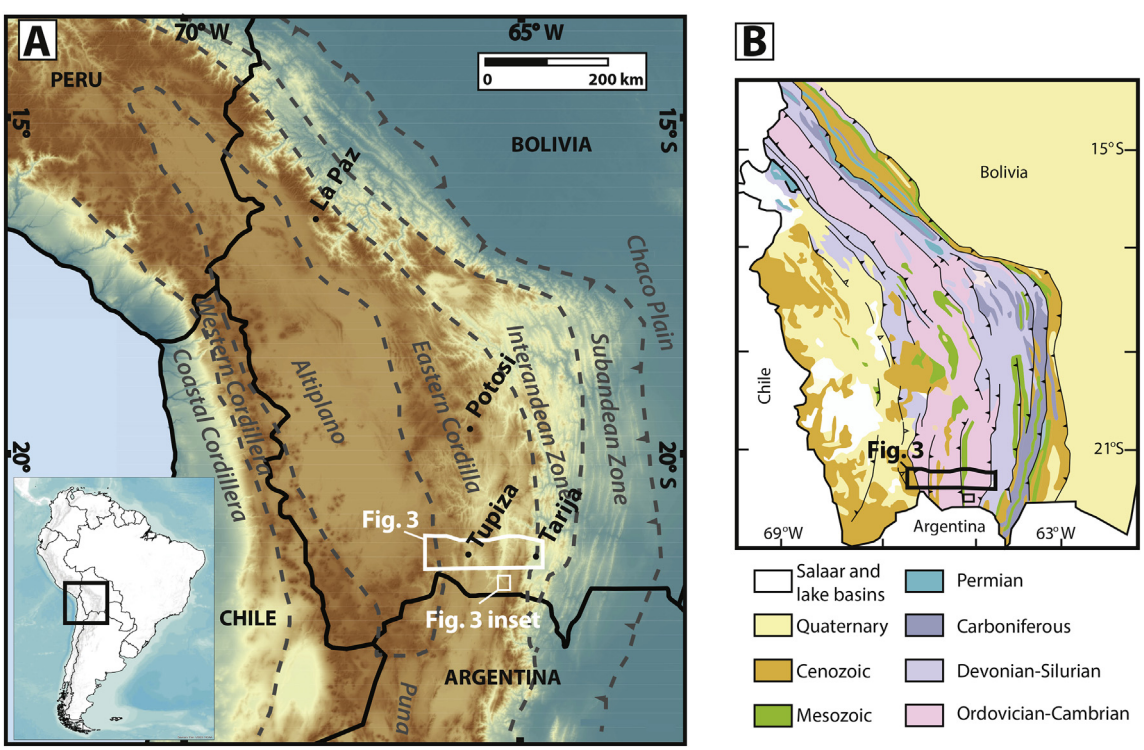

Fig. 2. A) Topography of the central Andes; dashed gray lines mark the boundaries of tectonomorphic zones (modified from Anderson et al., 2017). B) Generalized geologic map of Bolivia (modified from McQuarrie, 2002; Eichelberger et al., 2013).

Paleozoic rocks are from vitrinite reflectance and illite-crystallinity data (Kley and Reinhardt, 1994; Jacobshagen et al., 2002), which are limited to temperatures between ~100 and ~ 300 °C (Mukhopadhyay, 1994; Merriman and Frey, 1999).

In this study, we present new peak temperature and deformation temperature estimates from Cambrian through Devonian rocks in and adjacent to the Eastern Cordillera in southern Bolivia, by utilizing Raman spectroscopy of carbonaceous material (RSCM) thermometry (e.g., Beyssac et al., 2002, 2003) and semi-quantitative bracketing constraints from quartz recrystallization microstructures (e.g., Stipp et al., 2002). We also reconstruct basin thicknesses and Paleozoic structures in the Eastern Cordillera by modifying the balanced and restored cross sections of Anderson et al. (2017). Our new temperature data, along with published illite K—Ar (Jacobshagen et al., 2002) and zircon fission track and (U—Th)/He ages (Anderson et al., 2018), are placed in a detailed structural context, which allows us to quantify regional metamorphic field gradients and construct temperature-time thermal models that provide insights into the timing and conditions of Paleozoic orogenesis. We then explore the implications of this work for the tectonic history of the western margin of Gondwana at this latitude.

2. Regional geologic background

The western edge of the South American Continent has been the site of periodic cycles of subduction and related tectonic activity for >500 Myr (e.g., Coney and Evenchick, 1994; Cawood, 2005; Cawood et al., 2009; Ramos, 2009; McGroder et al., 2015). The present-day Andean mountain belt is the result of Late Cretaceous to Cenozoic deformation driven primarily by subduction of the oceanic Nazca plate beneath the South American continent and major changes in relative or absolute plate motion (e.g., Allmendinger et al., 1997; Coney and Evenchick, 1994; Isacks, 1988; Maloney et al., 2013; Horton, 2018a, 2018b; Martinod et al., 2020). The central part of the Andes (~14–24°S) has been divided into distinct tectonomorphic zones (e.g., Isacks, 1988; Kley, 1996; McQuarrie, 2002), including the Coastal Cordillera, the active volcanic arc of the Western Cordillera, and the retroarc region divided into the Altiplano, Eastern Cordillera (EC), Interandean zone (IAZ), Subandean zone (SAZ), and Chaco Plain (Fig. 2). The central Andes at the latitude of Bolivia and Northern Chile have accommodated the highest magnitude of crustal shortening during Cenozoic fold-thrust belt development (>300 km; e.g., McQuarrie, 2002; Arriagada et al., 2008; Eichelberger and McQuarrie, 2015; Anderson et al., 2017), which has overprinted the deformation record of earlier tectonic events. In this paper, we focus primarily on Paleozoic metasedimentary rocks within the EC and the adjacent margins of the Altiplano and IAZ (Fig. 3).

2.1. Stratigraphy of the Eastern Cordillera and adjacent zones

The EC in southern Bolivia is comprised of an ~8–12 km-thick section of Late Cambrian to Late Ordovician, low-grade (anchizone-epizone) metasedimentary rocks (Sempere, 1995; Egenhoff et al., 2002; Jacobshagen et al., 2002; Müller et al., 2002), which are unconformably overlain by nonmetamorphosed Mesozoic and Cenozoic sedimentary rocks (Gubbels et al., 1993; Kennan et al., 1997; Horton, 1998, 2005; DeCelles and Horton, 2003). This same relationship is observed along-strike in northern Argentina and central-northern Bolivia (Mon and Salfity, 1995; McQuarrie, 2002; Eichelberger et al., 2013). Along our studied transect at ~21°S, the oldest rocks are Upper Cambrian quartzites exposed in the core of the Cuesta de Sama anticlinorium on the eastern side of the EC (Fig. 3). Ordovician rocks consist of a monotonous turbiditic section composed primarily of slate with intercalated sandstone and quartzite that is up to ~11 km thick (Sempere, 1995; Müller et al., 2002; Egenhoff, 2007). The EC can be further divided into three segments given that only Upper Ordovician rocks are exposed in the western part of the EC, while Middle and Lower Ordovician rocks are exposed in the central part, and Lower Ordovician rocks are exposed in the eastern part (Maletz and Egenhoff, 2001; Jacobshagen et al., 2002; Müller et al., 2002; Egenhoff, 2007; Egenhoff et al., 2002, 2004). Due to Cenozoic contractional deformation, a complete Ordovician section is not exposed at any one locality in the EC and the original stratigraphic relationships between Lower, Middle, Upper Ordovician rocks are unknown (Müller et al., 2002).

Silurian through Permian rocks are not exposed within the EC at this latitude, but are observed at the surface or in wells within the adjacent parts of the Altiplano and IAZ. In the southeastern Altiplano, a minimum of ~2.8 km of Silurian and Devonian rocks below an unconformity with Upper Cretaceous strata have been documented in well logs (Welsink et al., 1995a). At the EC-IAZ boundary, > ~ 3 km of Silurian-Devonian sandstone and shale disconformably overlie Lower Ordovician rocks (Sempere, 1995; Kley, 1996; Anderson et al., 2017). Carboniferous-Permian rocks within the IAZ consist of a < ~1.2 km-thick section of sandstone, diamictite, dolomite, and shale (Fig. 3). The Carboniferous section tapers westward from ~2.4 km-thick in the Chaco Plain to <~0.5 km-thick at the EC-IAZ boundary (Kley, 1996; Anderson et al., 2017), which suggests that the EC was a paleotopographic high in the late Paleozoic (e.g., Starck, 1995; Tankard et al., 1995). The Permian section is ~0.6 km-thick and is exposed across the SAZ, and IAZ (Tröeng et al., 1993; Dunn et al., 1995), but is not observed in the EC at this latitude.

The Mesozoic section consists primarily of a ~ 0.5 km-thick section of uppermost Cretaceous (~63–70 Ma) marine sedimentary rocks that is regionally correlative across the EC and Altiplano (Welsink et al., 1995b; Sempere et al., 1997; Horton et al., 2001). In addition, a > 1 km-thick section of sandstone, mudstone, and intercalated basalt is exposed in a narrow N-S outcrop belt near the town of Tupiza, and may be related to Early to Middle Mesozoic rifting and post-rift thermal subsidence focused along the axis of the central EC (Horton, 1998; Müller et al., 2002; Sempere et al., 2002). The regional sub-Mesozoic unconformity in the EC is best exposed along the eastern side of the Camargo Syncline (Fig. 3), where Upper Cretaceous strata overlie Lower Ordovician rocks with up to 10–20° of difference in dip angle (Fig. 4A-C; Müller et al., 2002). However, the stratigraphic level below the unconformity varies across- and along-strike, as Upper Cretaceous rocks overlie Devonian rocks in the eastern Altiplano (Welsink et al., 1995a), Triassic-Jurassic rocks overlie Middle Ordovician rocks in the Tupiza region (Müller et al., 2002), and Mesozoic rocks overlie Silurian and Devonian rocks in the EC in central and northern Bolivia (~20–17°S; McQuarrie, 2002; Eichelberger et al., 2013). At 21°S, the unconformity records significant across-strike gradients in erosion magnitude as well. For example, the > ~ 4 km-thick Silurian–Permian section exposed along the IAZ-EC boundary is missing in the hinge zone of the Camargo syncline ~50 km to the west (Kley, 1996; Anderson et al., 2017) (Fig. 3).

Cenozoic rocks include ~3 km of Paleogene deposits of the Andean foreland basin (DeCelles and Horton, 2003) and ~ 0.5–2.5 km of Neogene intermontane basin deposits (Horton, 1998, 2005; Müller et al., 2002), which are in turn beveled by the ~10–12 Ma San Juan del Oro regional erosional surface (Gubbels et al., 1993; Kennan et al., 1997).

2.2. Paleozoic tectonic overview

Following the Neoproterozoic rifting of Rodinia and the initial opening of the ancestral Pacific Ocean basin, major plate reorganization and the final amalgamation of Gondwana was accompanied by a switch to a convergent plate boundary setting along the Pacific margin by ~570 Ma (Fig. 1, Cawood, 2005; Cawood and Buchan, 2007). Protracted cycles of convergence and subduction throughout the Paleozoic resulted in construction of the Terra Australis Orogen, a long lived accretionary orogen along the entire length of South American proto Pacific margin (Cawood, 2005; Cawood et al., 2009). Distinct orogenic pulses (e.g., Tilaric, Pampean, Famatinian, Ocloyic, Chañic) are recorded along individual segments the Terra Australis, culminating with the final

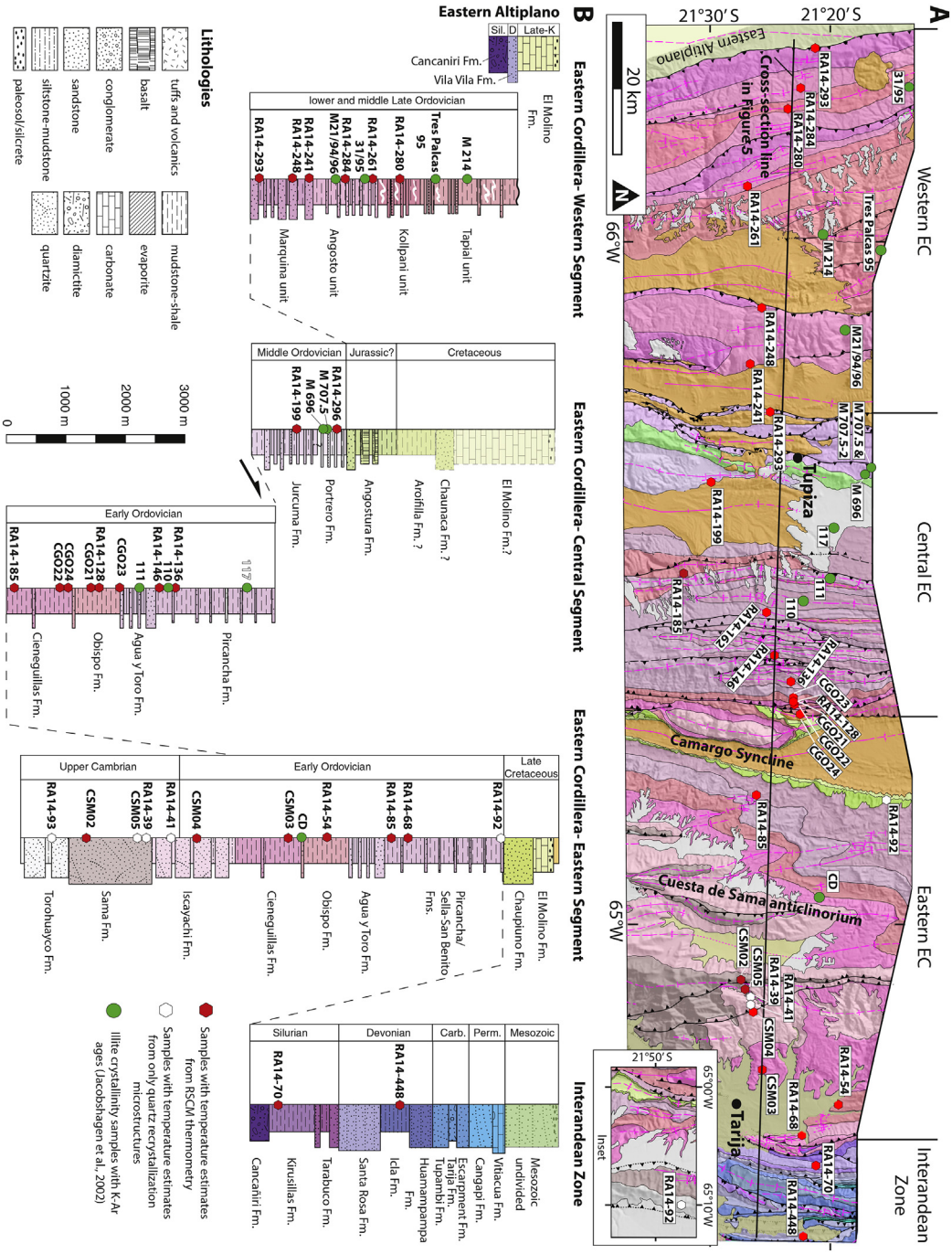

Fig. 3. A) Geologic map of the eastern Altiplano, Eastern Cordillera (EC), and western Interandean Zone between ~21°40′S and 21°10′S (modified from Anderson et al., 2017), with locations of RSCM and quartz recrystallization microstructure samples from this study and published illite crystallinity and illite K—Ar samples from Jacobshagen et al. (2002) shown. B) Stratigraphic columns of the eastern Altiplano, EC, and Interandean Zone with samples from this study and published samples plotted (modified from Dunn et al., 1995; Sempere, 1995; Welsink et al., 1995; Horton, 1998; Müller et al., 2002; DeCelles and Horton, 2003; Uba et al., 2006; Elger et al., 2005; Egenhoff, 2007; Anderson et al., 2017). Colors correspond with formation age divisions used for the map shown in A. The stratigraphic columns are restored to a pre-Cenozoic horizontal datum defined by regionally correlative uppermost Cretaceous paleosols and silcretes in the El Molino Formation and equivalents (e.g., Kley, 1996; Anderson et al., 2017).

assembly of Pangea and the onset of the Carboniferous to Mesozoic Gondwanide Orogeny (Cawood, 2005; Cawood et al., 2009; Heredia et al., 2018). The style, geometry, and intensity of Gondwanide deformation varies along the length of the orogen, but is marked in the central and southern Andes by fold-thrust deformation, the beginning of a major subduction cycle, and transpression during advance of the accretionary orogen (Bahlburg and Hervé, 1997; Ramos and Aleman, 2000; Cawood, 2005; Kleiman and Japas, 2009; Heredia et al., 2018; Oriolo et al., 2019).

Early convergence along the western margin of Gondwana was marked by episodes of terrane accretion and collisional deformation in the Cambrian (Pampean and Tilcaric Orogenies), followed by development of a subduction zone and establishment of the Ordovician (~490–460 Ma) Famatinian arc (Ramos, 2008, 2018; Pearson et al., 2012; Einhorn et al., 2015; Rapela et al., 2018). Cessation of Famatinian arc magmatism coincided with the ~465–460 Ma accretion of the Cuyania-Precordillera terrane to the western margin of northern Chile and Argentina (Ramos, 2008), which was accompanied by crustal

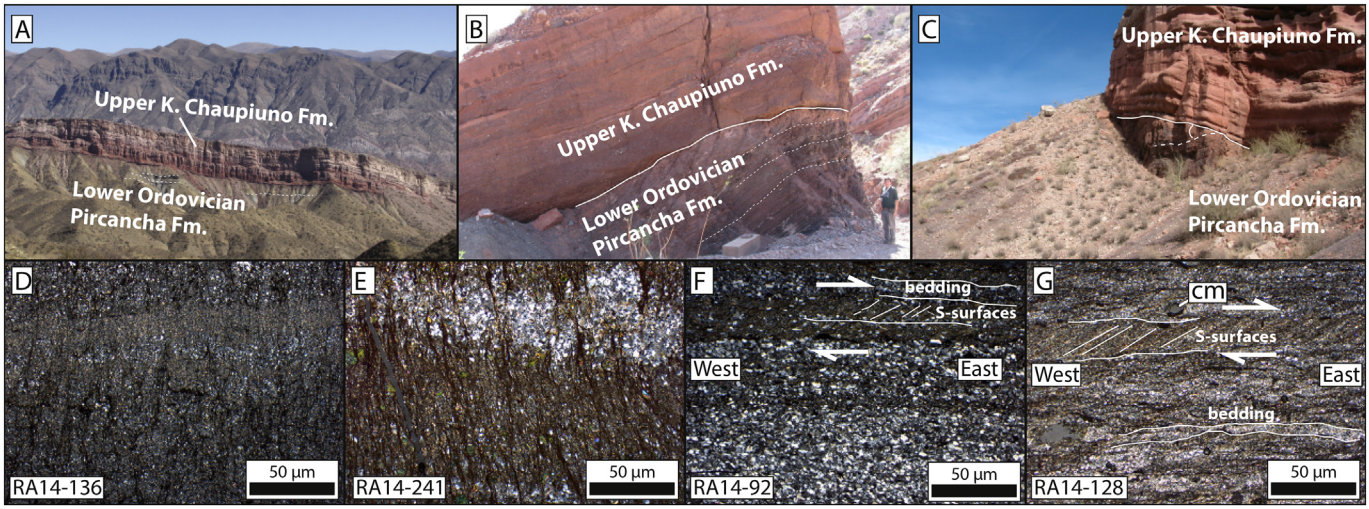

Fig. 4. A-C) Field photographs illustrating the unconformity between Lower Ordovician and Upper Cretaceous rocks along the eastern side of the Camargo Syncline at ~21°25′ S (A&B) and ~ 21°50′ S (C). Annotated bedding in Ordovician rocks shows that the unconformity varies between ~0° to 20° of difference in dip angle above and below. D-E) Photomicrographs (cross-polarized light) of penetrative, bedding-subnormal cleavage in the Lower Ordovician Pircancha Formation (sample RA14–136) and Upper Ordovician Angosto Formation (sample RA14–241). F-G) Photomicrographs (cross-polarized light) of top-to-the-east SC fabrics developed in the Lower Ordovician Pircancha Formation (sample RA14–92) and Lower Ordovician Obispo Formation (sample RA14–128).

shortening in the EC of northwestern Argentina and elsewhere in the Sierras Pampeanas during the Late Ordovician to Silurian Ocloyic orogeny (Coira et al., 1982; Mon and Hongn, 1991; Mon and Salfity, 1995; Astini and Dávila, 2004).

After cessation of the Ordovician Famatinian arc, the present-day EC was part of a mid-Paleozoic backarc or retrowedge region located to the east of a tectonic highland known as the Transpampean arch (Tankard et al., 1995; Starck, 1995; McGroder et al., 2015). The lack of Silurian to Carboniferous volcanic rocks in the western central Andes suggests that arc magmatism paused for ~100 Myr, and that the western edge of Gondwana at these latitudes was possibly a passive or strike-slip margin (Bahlburg and Hervé, 1997). However, Silurian-Devonian clastic sediment continued to be shed eastward from the Transpampean arch into a basin located in the present-day EC, IAZ, and SAZ (Isaacson, 1975; Isaacson et al., 1995; Isaacson and Díaz Martínez, 1995; Tankard et al., 1995; McGroder et al., 2015; Calle et al., 2017; Koltonik et al., 2019).

Late Paleozoic deformation, variably referred to as being related to either the Chañic (Mon and Salfity, 1995), Hercynian (Jacobshagen et al., 2002), or Gondwanide orogeny (Ramos, 2018), is evident across the central Andes from regionally extensive unconformities between Carboniferous rocks and underlying deformed Paleozoic rocks (e.g., Bahlburg et al., 1987; Mon and Hongn, 1991; Welsink et al., 1995b; Espurt et al., 2008; McGroder et al., 2015). However, in the EC in southern Bolivia and northern Argentina, middle to late Paleozoic deformation is more difficult to identify because of the lack of Devonian-Carboniferous rocks and the broad timespan missing across the unconformity between Ordovician and Upper Cretaceous rocks (McGroder et al., 2015).

In southern Bolivia, Paleozoic rocks dominantly reflect the sedimentary record of tectonic activity after the Cambrian Pampean Orogeny. Although Famatinian arc and related metamorphic rocks are exposed along much of the Andes from ~30°S to ~6°S, they are notably absent from the Altiplano and EC from southern Bolivia (~22°S) to central Peru (~13°S) (Ramos, 2018). Nevertheless, the EC at these latitudes is thought to have occupied a backarc setting as early as Late Cambrian (Coira et al., 1999; Astini and Dávila, 2004; Egenhoff, 2007; Ramos, 2018). Subsidence studies identify two stages during accumulation of the anomalously thick Late Cambrian–Ordovician section in the Famatinian backarc basin of Bolivia, consisting of an early stage of extension-related thermal subsidence followed by generation of a flexural foreland basin related to growth of an orogenic highland to the west (Egenhoff, 2007; Ramos, 2008).

Although Silurian through Carboniferous rocks are not preserved in the EC south of ~20°S, sedimentary facies and provenance studies of these rocks in the IAZ, SAZ, and Chaco Plain suggest that they may represent an eastward-migrating foreland basin system that continued after shutdown of the Famatinian arc (Gohrbandt, 1993; Sempere, 1995; Isaacson et al., 1995; Isaacson and Díaz Martínez, 1995; Calle et al., 2017). Periodic contractional or transpressional deformation along the Gondwanan margin and the resulting expansion of the Transpampean highland toward the continent interior, which swept eastward across the proto-Andes from at least the Middle Silurian into the late Paleozoic, is inferred to be the driver of flexural subsidence (McGroder et al., 2015). However, an alternative viewpoint is that the absence of Silurian-Carboniferous rocks in the EC of northern Argentina and southern Bolivia reflects a remnant Ordovician highland that persisted through most of the Paleozoic following cessation of back-arc subsidence after the Ocloyic orogeny (e.g., Starck, 1995).

Metamorphism and cleavage development exhibited by Cambrian-Ordovician rocks, as well as the development of the unconformity between Ordovician and Mesozoic strata in the EC of southern Bolivia, are variably attributed to the Ocloyic or other late Paleozoic orogenic events (e.g., Kley and Reinhardt, 1994; Kley et al., 1997; Sempere, 1995; Starck, 1995; Jacobshagen et al., 2002; Müller et al., 2002; McGroder et al., 2015). The rocks below the unconformity exhibit penetrative, bedding-subnormal, continuous to spaced cleavage (Fig. 4D-E), along with top-to-the-east shear-sense indicators (Fig. 4F-G), which define an episode of contractional deformation prior to the Late Cretaceous (Sempere, 1995; Kley et al., 1997; Müller et al., 2002). Lower Paleozoic rocks in the EC were metamorphosed to prehnite-pumpellyite and lower greenschist-facies conditions (Kley and Reinhardt, 1994; Jacobshagen et al., 2002), which are similar to the deformational conditions experienced by lower Paleozoic rocks in northwestern Argentina during the Late Ordovician Ocloyic orogeny (e.g., Coira et al., 1982; Astini and Dávila, 2004). Because of this similarity, development of cleavage in Ordovician rocks in Bolivia south of ~20°S has often been attributed to the Ocloyic orogeny (Sempere, 1995; Allmendinger et al., 1983; Ramos, 2008). However, others suggest that fabrics and the development of the unconformity above Ordovician

rocks in southern Bolivia was related to orogenesis that culminated in the Late Carboniferous (Kley and Reinhardt, 1994; Kley et al., 1997; Jacobshagen et al., 2002; Müller et al., 2002). Illite crystallinity and vitrinite reflectance, 320–290 Ma K-Ar ages on *syn*-kinematic illite, and across-strike changes in the upper Paleozoic strata point to a deformation event that may have begun by Late Devonian and lasted into the Early Permian (Kley and Reinhardt, 1994; Kley et al., 1997; Jacobshagen et al., 2002; Müller et al., 2002; Anderson et al., 2017), and zircon (U—Th)/He ages from Ordovician samples not reset by Cenozoic burial record a period of exhumation during the Late Carboniferous (Anderson et al., 2018).

Nevertheless, the metamorphism, cleavage development, and erosion that pre-dates deposition of Upper Cretaceous rocks may still be a combination of Ordovician Ocloyic, late Paleozoic deformation, or early to middle Mesozoic rifting. Additionally, several problems that confound a clear understanding of the timing and thermal conditions of Paleozoic orogenesis remain unresolved. For example, the rocks that the illite crystallinity, vitrinite reflectance, and illite K—Ar data were collected from were not restored to a pre-Andean configuration, so the modern across-strike patterns of metamorphic age, zonation, and thermal structure are not an accurate representation of Paleozoic conditions. Furthermore, new insights into the illite/muscovite Ar system show that closure of illite K—Ar ages occurs at temperatures above ~300 °C (Harrison et al., 2009; Rahl et al., 2011; Verdel et al., 2012), suggesting that the published illite crystallinity data may underestimate the peak temperatures of Paleozoic rocks in the EC. Below, we attempt to resolve this problem by quantifying the thermal conditions and timing of cooling of rocks below the unconformity.

3. Structural and stratigraphic context of temperature samples

A suite of 31 samples from Cambrian to Devonian metasedimentary rock units (Figs. 3, 5) were analyzed to quantify peak temperatures and deformation temperature conditions during low-grade metamorphism. Samples were collected within the map area of Anderson et al. (2017) along an east-west transect that spans across the EC at ~21°S. We also compiled published illite crystallinity temperatures paired with illite K—Ar ages (Jacobshagen et al., 2002), as well as zircon (U—Th)/He (ZHe) and zircon fission track (ZFT) cooling ages (Anderson et al., 2018) along the same transect, in order to constrain thermal models that provide new timing constraints on exhumation.

3.1. Structural restoration of sample burial

Samples are given structural and stratigraphic depth context by projecting them to their present-day location on the balanced cross section of Anderson et al. (2017), and by performing a two-step restoration to their original Paleozoic position (Fig. 5). First, Cenozoic shortening was removed and the cross section was restored to a well-constrained Late Cretaceous configuration (Fig. 5B, annotation 1) using the regionally extensive limestone, paleosol, and silcrete layers in the El Molino and Ichoa Formations as a continuous, low-elevation surface that spanned from the Altiplano to the SAZ (e.g., Kley, 1996; Anderson et al., 2017 and annotations therein). Samples restored to this horizontal datum span stratigraphic burial depths of ~0–6 km below the base-Cretaceous unconformity (Fig. 5B).

Sample positions prior to the Mesozoic are more difficult to reconstruct due to uncertain stratigraphic relationships between Lower, Middle, and Upper Ordovician rocks (Fig. 3B) (Müller et al., 2002; Egenhoff, 2007), and the unknown amount of Silurian-Carboniferous overburden in the EC prior to the Mesozoic (Fig. 3A). However, restoration to the uppermost Cretaceous El Molino-Ichoa Formation base level (Fig. 5B) revealed at least five large-scale structural features developed in the Paleozoic and early Mesozoic, which when restored to an undeformed geometry provide important insights into the original basin configuration (see annotations on Fig. 5). The oldest structure is an early Paleozoic normal fault inferred along the eastern margin of the EC (Fig. 5, annotation 4). This structure is interpreted on the basis of major east-west thickness changes illustrated by geophysical data, which show that Silurian rocks likely overlie crystalline basement in the IAZ and SAZ (Kley et al., 1996), but overlie nearly ~8 km of metasedimentary Cambrian-Ordovician rocks at the EC-IAZ boundary (Kley, 1996; Anderson et al., 2017). Additionally, sedimentary facies within Lower Paleozoic rocks in the EC are indicative of a transgressive sequence that was deposited in a rapidly subsiding and widening extensional basin that filled from the east (Sempere, 1995; Egenhoff, 2007).

Paleozoic structures developed after the Late Ordovician include an east-vergent monocline at the EC-IAZ boundary (Fig. 5B, annotation 5), a west-vergent monocline in the western EC (Fig. 5B, annotation 6), and an east-vergent thrust fault concealed beneath the Camargo syncline (Fig. 5B, annotation 3) (Anderson et al., 2017). Along the eastern margin of the EC, ~3.5 km of Silurian through Carboniferous rocks disconformably overlie Lower Ordovician rocks in the eastern limb of the Cuesta de Sama anticlinorium but are missing in the western limb of the fold (Fig. 5A). Reactivation and inversion of the aforementioned Early Ordovician normal fault as an east-vergent reverse fault is interpreted to have produced the monoclinal structure (Fig. 5B, annotation 5). This structural inversion is interpreted to have resulted in the development of an erosional high in the eastern EC, and explains the erosion of the upper Paleozoic section over such a short (~50 km) east-west distance (Kley, 1996; Anderson et al., 2017). Similarly, the west-vergent monocline in the western EC is interpreted from major east-west variations in the preserved thickness of the Upper Ordovician section (Müller et al., 2002; Anderson et al., 2017). In the central EC, Middle Ordovician rocks are disconformably overlain by Jurassic sandstones (Kley et al., 1997; Sempere et al., 2002), but a > 6 km-thick section of Upper Ordovician to Lower Silurian rocks are present below the base-Cretaceous unconformity in the western EC and eastern Altiplano (Welsink et al., 1995b; Müller et al., 2002; Anderson et al., 2017). Field relationships reveal the third Paleozoic structure concealed beneath the Camargo syncline, where Ordovician rocks below the Cretaceous unconformity on the western limb of the fold are ~2–3 km stratigraphically lower than the Ordovician rocks below the unconformity on the eastern limb (Servicio Geológico de Bolivia, 1992). This field relationship indicates that Ordovician rocks must dip moderately westward below the unconformity on the western limb (Fig. 3A); therefore, the concealed structure is depicted as an east-vergent thrust fault (Anderson et al., 2017) (Fig. 5B).

The final major structure is a pre-Cretaceous normal fault in the central EC (Fig. 5, annotation 2). Rift-related sedimentary basins and associated magmatism define Permian through Jurassic development of a narrow extensional corridor along the axis of the EC from Peru to southern Bolivia (Sempere et al., 2002). Near the town of Tupiza (Figs. 3A, 5A), tight synclinal folding of Jurassic rift-related deposits (Angostura Fm.) relative to more gently folded Cenozoic rocks is attributed to an east-vergent footwall breakthrough of an inverted normal fault at the Jurassic-Ordovician contact in the eastern limb of the fold (Kley et al., 1997; Sempere, 2000; Müller et al., 2002). However, no obvious fault could be located along the eastern edge of the syncline (Hérail et al., 1996; Horton, 1998, 2000; Anderson et al., 2017). Instead, it was proposed that if a normal fault is present, it is concealed beneath the Cenozoic cover to the east and is interpreted to have accommodated a minimal amount of extension and later inversion (Anderson et al., 2017).

Excluding the Early Ordovician normal fault (Fig. 5B, annotation 4), retro-deforming the Paleozoic contractional structures and the Mesozoic normal fault restores samples to their general position during Paleozoic time. Nevertheless, several assumptions must be made regarding the thicknesses of Ordovician through Devonian rocks in order to arrive at the final cross-section configuration and estimated sample burial depths prior to deformation (Fig. 5C, annotations 7–9). The stratigraphic thicknesses estimated herein are the final compacted

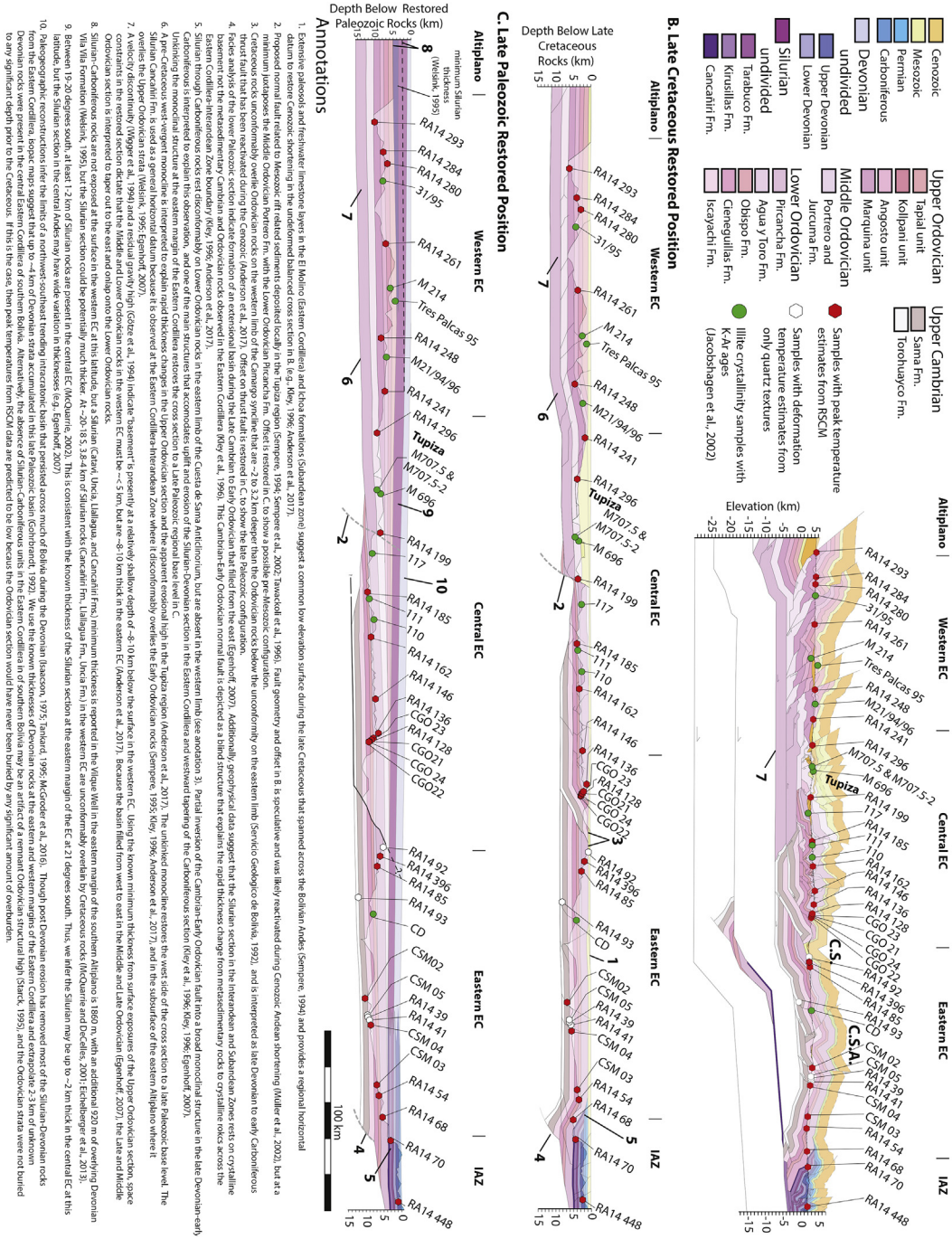

Fig. 5. Line-length balanced deformed and restored cross sections across the Eastern Cordillera with annotated footnotes. A and B are modified from Anderson et al. (2017). Samples shown on Fig. 3 are projected into the cross section. A) Present-day geometry resulting from Cenozoic Andean shortening. B) Restored geometry at the end of the Late Cretaceous; note the pre-Late Cretaceous structures revealed by this restoration. C) Interpreted late Paleozoic cross-section reconstruction. Abbreviations: C.S. = Camargo Syncline; C.S.A. = Cuesta de Sama Anticlinorium, EC = Eastern Cordillera.

thicknesses, compaction through time and with increasing burial is not accounted for.

Due to Cenozoic shortening, the Lower, Middle, and Upper Ordovician sections are only observed in fault contact with one another, so the original stratigraphic relationships of the entire Ordovician succession are uncertain (Müller et al., 2002). The present-day thickness of the preserved Ordovician section is well-constrained from geophysical data and field relationships (Götze et al., 1994; Wigger et al., 1994; Müller et al., 2002; Servicio Nacional de Geología y Técnico de Minas, 2010; Anderson et al., 2017), which show that Middle and Lower Ordovician rocks are much thinner in the western EC (~ < 5 km) than in the eastern EC (~8–10 km). Given that the thick Upper Ordovician section (>6 km) is only present in the western EC, we interpret that the Upper Ordovician strata taper eastward and onlap onto Middle and Lower Ordovician rocks (Fig. 5C, annotation 7).

The thickness of the Silurian through Carboniferous section is assumed primarily from exposures along the margins of the EC, well data in the eastern Altiplano, and exposures of Silurian-Devonian rocks preserved farther north (20–18°S). A minimum thickness of ~2.8 km in the western EC is inferred from the subsurface thickness of

Silurian and Devonian rocks encountered in a well at the eastern margin of the southern Altiplano (Fig. 5, annotation 8; Welsink et al., 1995b), which is comparable to the ~3 km-thick Silurian-Devonian section observed east at the EC-IAZ boundary. However, the Silurian section was likely much thicker in the west given that a considerably thicker (~4 km) Silurian section is observed in the western EC in central Bolivia (~18–20°S; McQuarrie and DeCelles, 2001; Eichelberger et al., 2013). Less is known about the thicknesses of upper Paleozoic rocks (Devonian-Permian) because there are few outcrops preserved within the EC. A ~ 1–2 km-thick section of Devonian rocks underlies Mesozoic rocks in the Incapampa Syncline within the eastern EC at ~19.5°S (McQuarrie, 2002), but isopach maps suggest that up to ~4 km of Devonian rocks may have accumulated in the Paleozoic basin (Gohrbandt, 1993). We use the known thicknesses of Devonian rocks at the eastern and western margins of the EC to extrapolate a reasonable estimate (~2–3 km) for the central EC at ~21°S (Fig. 5, annotation 10). The Carboniferous section tapers westward from ~2.5 km thick in the Chaco Plain to <0.5 km-thick at the EC-IAZ boundary (Tröeng et al., 1993; Anderson et al., 2017), and is not preserved anywhere in the EC of southern and cental Bolivia (McQuarrie, 2002; Eichelberger et al., 2013). Additionally, Carboniferous rocks are interpreted to have been deposited in a retroarc setting, sourced from a structural high in the west, potentially in the EC and Altiplano (Isaacson, 1975; Isaacson et al., 1995; Tankard et al., 1995; McGroder et al., 2015; Calle et al., 2017; Koltonik et al., 2019). Therefore, we assume that an appreciable thickness of Carboniferous rocks was never deposited in the EC.

Alternatively, the absence of Silurian-Carboniferous units in the EC at ~21°S may be the result of an Ordovician structural high that persisted until Late Cretaceous time (Starck, 1995). Though this scenario is unlikely given the illite crystallinity and vitrinite reflectance temperatures from Paleozoic rocks immediately below the unconformity (e.g., Kley and Reinhardt, 1994; Jacobshagen et al., 2002), we explore this possibility in greater detail in the subsequent temperature data and discussion sections.

From the reconstructed cross section, we estimate total Paleozoic stratigraphic thicknesses up to ~13–15 km in the western and central EC, and ~ 11 km in the eastern EC (Fig. 5C). Our samples spanned a restored east-west distance of ~300 km prior to Paleozoic and Cenozoic shortening events, and were exhumed from original stratigraphic depths primarily between ~5 and ~ 11 km.

4. Peak and deformation temperature data

4.1. Deformation temperature ranges from quartz recrystallization microstructures

The morphology of dynamically recrystallized quartz can be utilized to provide a semi-quantitative estimate of the deformation temperature range of recrystallization (e.g., Stipp et al., 2002; Law, 2014), and to offer a comparison with quantitative peak temperature estimates from RSCM thermometry (e.g., Long and Soignard, 2016; Long et al., 2016, 2017). Microstructures and textures associated with dynamic recrystallization of quartz have been correlated with experimentally derived dislocation creep regimes over a temperature range of ~250–700 °C (Stipp et al., 2002). Following the criteria for identifying quartz recrystallization microstructures outlined in Stipp et al. (2002), thin sections from all 31 samples were examined for evidence of undulose extinction, crystal-plastic elongation, and recrystallization of quartz. Photomicrographs of representative microstructures are illustrated in Fig. 6. Results from all samples are shown in Table 1 and are plotted to a restored depth below the reconstructed top of the upper Paleozoic section.

All samples except Devonian sample RA14–448 contain quartz grains that exhibit undulose extinction (Fig. 6A-B), and some samples contain quartz clasts isolated in a micaceous matrix that exhibit evidence for elongation sub-parallel to cleavage (Figs. 6B-C). Minimum deformation temperatures of ~250–270 °C are required for crystal-plastic deformation and development of undulose extinction in quartz (e.g., Dunlap et al., 1997; van Daalen et al., 1999; Stipp et al., 2002). Therefore, our observations suggest that all samples in the EC except one achieved deformation temperatures greater than ~250 °C. We recognize the potential for recycled quartz grains with undulose extinction, but because samples exhibit shape-preferred elongation of quartz parallel to foliation and/or cleavage, we consider undulose extinction in quartz to be a product of in situ deformation.

Ten samples exhibited evidence of bulging recrystallization (BLG) (e.g., Bailey and Hirsch, 1962; Drury et al., 1985; Drury and Urai, 1990), which occurs at an approximate deformation temperature of ~280–400 °C (Stipp et al., 2002). In these samples (Table 1), adjacent quartz grains exhibit bulbous grain boundaries <~5 μm in diameter (Fig. 6D-H). BLG was only observed for samples with Paleozoic burial depths greater than ~6.5 km, though not every sample below this depth exhibited these microstructures. As this technique gives semi-quantitative information on deformation temperature rather than peak temperature, these observations do not preclude samples having attained higher peak temperatures. Dynamic recrystallization fabrics in quartz commonly develop during subsequent retrograde conditions, and often record deformation temperatures that are well below peak metamorphic temperatures (e.g., Law et al., 2013, Long et al., 2016; Hunter et al., 2018; Starnes et al., 2020).

4.2. RSCM thermometry

RSCM thermometry can be used to quantify the peak metamorphic conditions that a rock achieved in a temperature range between ~100 and ~ 740 °C (e.g., Beyssac et al., 2002, 2003; Rahl et al., 2005), and has been applied in a variety of orogens and sedimentary basins (e.g., Cottle et al., 2011; Long and Soignard, 2016; Long et al., 2016, 2017; Baludikay et al., 2018; Starnes et al., 2020). Carbonaceous material (CM) is derived from the solid-state transformation of poorly ordered organic carbon into ordered graphite bonds during metamorphism, which is highly dependent on temperature (Buseck and Huang, 1985). The RSCM thermometer is not influenced by retrogression and is a measure of peak conditions because the temperature-dependent organization of the CM structure is irreversible (Beyssac et al., 2002).

Temperatures were determined by measuring the height ratio (R1) and the area ratio (R2) of four first-order Raman peaks (G, D1, D2, D3) in the relative wavenumber range between 1200 and 1800 cm^{-1}, using Eqs. 1, 2, and 3 of Rahl et al. (2005). RSCM measurements were made at the LeRoy Eyring Center for Solid State Science at Arizona State University using a custom-built Raman spectrometer (see Supplementary Material, Text S1 for a detailed explanation of instrument parameters, settings, and procedures).

CM was measured in situ on 27 samples of Cambrian to Devonian metasedimentary rocks from across the EC (Fig. 7, Table 1). CM was abundant in most samples and was present dominantly as ~5–75 μm isolated patches, but also occurred as ~5–15 μm-thick laminations (Fig. 7A-G). To avoid structural defects introduced by sample preparation, the laser was focused on CM positioned beneath a transparent mineral grain (most commonly quartz) (e.g., Beyssac et al., 2002). Representative Raman spectra from each sample are shown in Fig. 7H, and the mean temperatures obtained from multiple spots analyzed from each sample are shown on Table 1 (see supplementary information, data in brief for data from each individual spot). Ideally, 10–15 spots were analyzed per sample in order to assess internal consistency; however, for some samples (RA14–261, RA14–199, RA14–92, CSM02, CSM03, CGO24) we were only able to obtain 3–9 spots. Following the procedure of Cooper et al. (2013), mean temperatures are reported at a 2 standard error (SE) level, which incorporates the internal uncertainty and external uncertainty (±50 °C) in the RSCM thermometer calibration of Rahl et al. (2005) (Table 1 footnote).

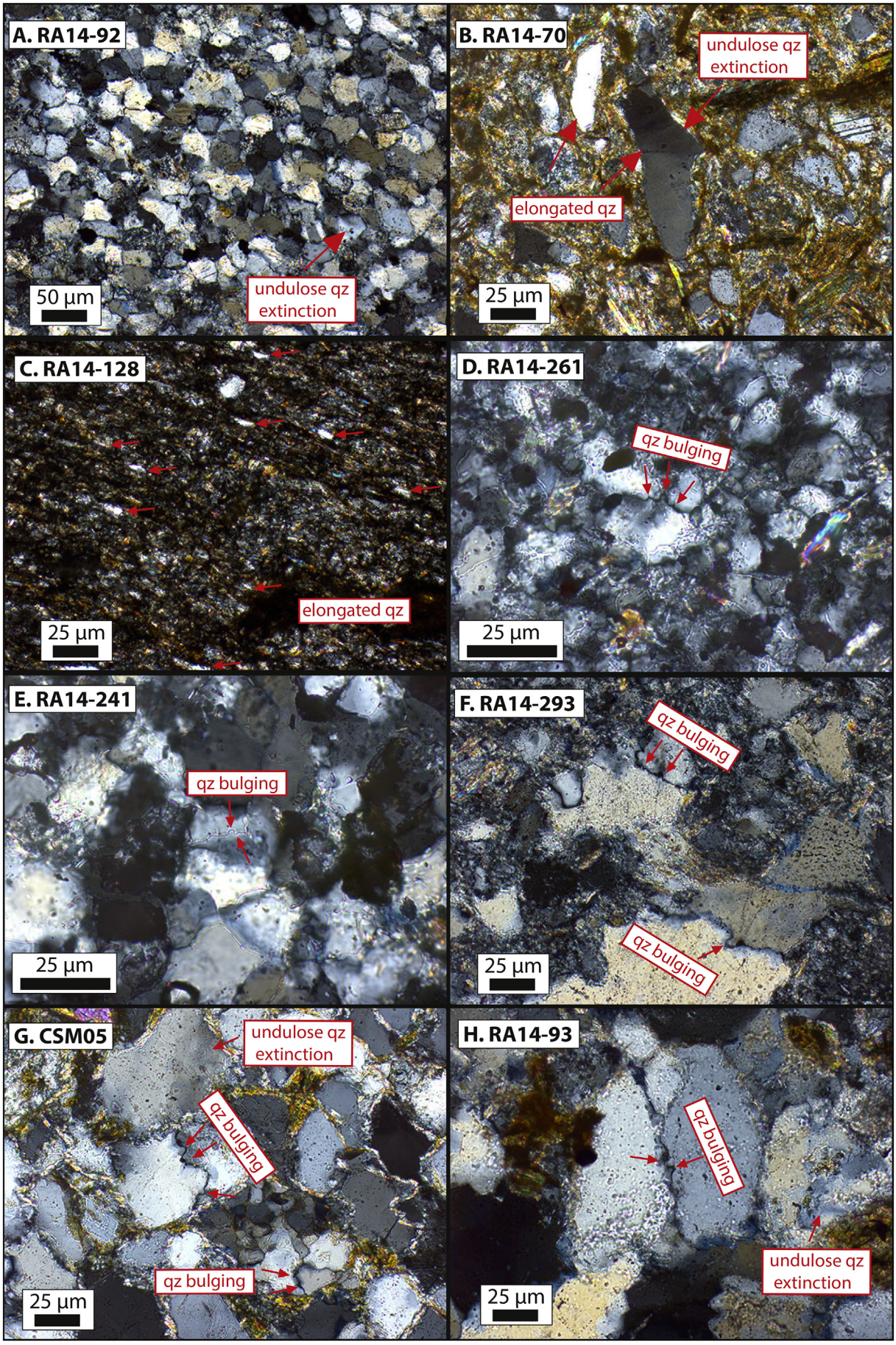
A. RA14-92
undulose qz extinction
50 µm
B. RA14-70
undulose qz extinction
elongated qz
25 µm
C. RA14-128
elongated qz
25 µm
D. RA14-261
qz bulging
25 µm
E. RA14-241
qz bulging
25 µm
F. RA14-293
qz bulging
qz bulging
25 µm
G. CSM05
undulose qz extinction
qz bulging
qz bulging
25 µm
H. RA14-93
qz bulging
undulose qz extinction
25 µm

The resulting RSCM peak temperatures ($n = 27$) range from ~220 to ~520 °C, with the majority ($n = 24$) between ~220 and ~ 400 °C (Table 1, Fig. 8). These data allow us to test whether the EC was a remnant Ordovician structural high that persisted until the Mesozoic (e.g., Starck, 1995). Plotting all the RSCM temperatures as a function of depth relative to the base-Cretaceous unconformity (Supplementary, data in brief Fig. 1A) results in samples at unrealistically high peak temperatures of 250–400 °C at relatively shallow depths (<2 km). Additionally, samples plotted by depth relative to this datum show a scattered pattern with no trend at 0–4 km depths and an unrealistic decrease in peak temperature at 4–6 km depths (Supplementary Fig. 1A). In contrast, samples plotted relative to the top of the reconstructed upper Paleozoic section exhibit some scatter but generally show a trend of increasing peak temperature with depth that falls within the bounds of typical geothermal gradients of 20–50 °C/km (Supplementary Fig. 1B). This is consistent with published illite crystallinity data and vitrinite reflection values, which illustrate a paleotemperature discontinuity between Upper Cretaceous strata and the underlying Ordovician metasedimentary rocks that can only be explained by removal of ~3–7 km strata prior to Mesozoic sedimentation (Kley and Reinhardt, 1994; Jacobshagen et al., 2002). Thus, we plot and interpret our data relative to the Paleozoic burial depths derived from our structural reconstruction (Fig. 8).

Given the large across-strike distance (~315 km restored east-west distance) and the distinct changes in stratigraphic exposure level across the western, central, and eastern EC, we further divide the RSCM results by location (Fig. 8). When classified by region, the samples display a more distinct trend of increasing RSCM temperature with Paleozoic burial depth. In the western EC, six samples from Upper Ordovician rocks span burial depths of ~6.5 to ~10 km and yielded RSCM temperatures between ~270 and ~ 350 °C (with one outlier, RA14–248, at ~472 °C) (Table 1). The peak temperature of sample RA14–248 is considerably higher than samples from similar depths in the western EC (e.g., RA14–261, RA14–284), and quartz recrystallization in this sample was not indicative of deformation at temperatures >400 °C.

In the central EC, 11 samples that span depths of ~7 to ~11 km were analyzed, and 10 of them yielded peak temperatures between ~220 and ~ 400 °C (Table 1). As with the western EC, one sample that yielded an anomalously high temperature (RA14–128, 520 °C) is suspect given that five adjacent samples yielded much lower RSCM temperatures.

In the eastern EC, the 14 analyzed samples span depths of ~1 to ~10 km, with RSCM temperatures between ~220 and ~ 420 °C (Table 1). Samples are primarily from Lower Ordovician and Cambrian rocks, but two samples are from Silurian (RA14–70) and Devonian formations (RA14–448). The shallowest sample (RA14–448) does not display undulose quartz extinction but yielded an RSCM temperature of 290 °C, despite a Paleozoic burial depth of ~1 km (Fig. 8). Except for this Devonian sample, peak temperatures of Cambrian-Silurian samples are in the ~220–420 °C range and generally increase with increasing Paleozoic burial depth. Additionally, no temperature discontinuity is observed across the disconformable contact between Lower Ordovician and Lower Silurian rocks (Figs. 3B, 8).

4.3. Temperature estimates from published illite crystallinity data

We compiled published illite crystallinity (IC) data collected at this latitude by Jacobshagen et al. (2002) and converted the reported IC values to a metamorphic temperature (e.g., Merriman and Frey, 1999; Zhu et al., 2016) in order to compare with our temperature estimates from RSCM and quartz recrystallization (Table 2). IC is a parameter that can be used to characterize the peak temperature conditions of low-grade pelitic rocks. IC works well for estimating peak temperatures of ~100 to 300 °C but may be limited in estimating temperatures > ~300 °C (Moore and Reynolds Jr., 1997; Merriman and Frey, 1999; Merriman and Peacor, 1999; Kübler and Jaboyedoff, 2000). IC values are determined by measuring the width of the basal 1-nm illite XRD peak at one-half of its height, reported in units of Δ°2Θ where°2Θ is the XRD angle (Kübler, 1967; Kübler and Jaboyedoff, 2000). The width of the 1-nm illite XRD peak and therefore the IC value are controlled primarily by temperature and decrease in value with increasing temperature (Ji and Browne, 2000). This relationship is used to illustrate variations in regional metamorphism and to define subgreenschist metapelitic zones (e.g., Verdel et al., 2011).

The across-strike distribution of IC values in the EC previously described by Jacobshagen et al. (2002), which included data from Manutsoglu et al. (1998), lacked location information and details on IC values. Manutsoglu et al. (1998) did not convert IC values to a metamorphic temperature and samples were not structurally restored to an original burial depth. Therefore, we focus our attention on the 10 samples for which Jacobshagen et al. (2002) reported location information and IC values (Table 2), so that the data can be projected into the cross section and restored to a reconstructed late Paleozoic burial depth. This includes one sample from the eastern EC (sample CD), five samples from the central EC (samples 110, 111, 117, M 696, M 701.5–2), and four samples from the western EC (samples M 21/94/96, Tres Palcas, M 214, 31/95) (Figs. 3, 5, 8). IC values for these samples are reported from two size fractions of illite, <2 μm and < 0.2 μm, accompanied by K—Ar ages for both size fractions (Jacobshagen et al., 2002). A common concern in IC analysis is whether illite within a sample is detrital or authogenic (Merriman and Frey, 1999). However, Late Devonian to Carboniferous K—Ar ages and consistency of ages of the two size fractions (e.g., coarser samples older than the smaller size fraction) from Ordovician shales in the EC (Jacobshagen et al., 2002) suggests that illite in these samples was newly formed and that IC values therefore reflect temperature conditions after deposition (e.g., Verdel et al., 2012).

Overall, the IC values range from 0.170 and 0.435°2Θ and define the metamorphic grade of the EC as generally upper anchizone to epizone conditions (prehnite-pumpellyite to lower greenschist-facies) (Jacobshagen et al., 2002). IC temperature estimates range from ~245 to ~355 °C (Table 2) and span Paleozoic burial depths of ~4.5 to ~10.5 km (Fig. 8). Temperature differences between the <2 μm and < 0.2 μm size fractions are typically < ~40 °C, and IC temperature estimates for both size fractions generally overlap within error, with RSCM peak temperatures from samples collected at similar depths (Fig. 8). Similar to the RSCM data, IC temperatures generally increase with depth, but show less scatter compared to the RSCM temperatures (Supplementary Fig. 1B). When separated by location, four samples of Upper Ordovician rocks from the western EC span burial depths of ~6.5 to ~10 km (Fig. 8), and correspond to temperatures of ~210–360 °C (Table 2). Five samples of Middle and Upper Ordovician rocks from the central EC span Paleozoic burial depths of ~7.5 to ~10.5 km (Fig. 8), and correspond to temperatures of ~240–350 °C. A single Lower Ordovician sample from the eastern EC (sample CD) restores to a Paleozoic burial depth of ~8 km (Fig. 8) and corresponds to temperatures of ~300–325 °C.

5. Discussion

Results from the three thermometry techniques presented above yielded similar temperature conditions of ~220 to ~400 °C for most

Fig. 6. Photomicrographs (cross-polarized light) illustrating representative examples of quartz (qz) recrystallization microstructures. A-B) Undulose extinction of quartz grains in the Lower Ordovician Pircancha Formation (A) and Silurian Kirusillas Formation (B). B—C) Foliation-subparallel, crystal-plastic elongation of quartz grains in the Lower Ordovician Obispo Formation. D—H) Examples of bulging recrystallization along quartz grain boundaries (in order of stratigraphic depth): Upper Ordovician Angosto Formation (D-E), Upper Ordovician Marquina Formation (F), Cambrian Sama Formation (G), and Cambrian Torohuayco Formation (H). See Table 1 for a summary all 31 samples analyzed for quartz microstructures.

Table 1
Peak and deformation temperature determinations from RSCM thermometry and quartz recrystallization microstructures.

	Sample	Map Unit	Restored structural depth (m)		R1		R2		Peak temperature (°C)				Quartz Texture		ZHe and ZFT cooling ages
			K.	Pz.	Mean	1σ	Mean	1σ	Mean	1σ	2 SE	n	Undulose	Bulging	
Eastern EC	RA14–92	Opi	0	5310	2.694	0.203	0.74	0.023	224	44	47	8	yes	–	88.3 ± 75.2 Ma (ZHe, ECO92), 262.5 ± 94.4 Ma (ZHe, ECO88)
	RA14–54	Oob	2420	6000	2.109	0.166	0.650	0.016	359	18	28	14	yes	–	95.6 ± 4.3 (ZHe, ECO53),91.0 ± 8.1 (ZHe, ECO56)
	RA14–68	Ose	4180	5220	1.076	0.152	0.693	0.027	248	11	31	11	yes	–	24.1 ± 1.5 (ZHe, ECO68)
	CSM03	Oci	3000	6560	2.003	0.246	0.671	0.027	336	98	40	9	yes	yes	–
	CSM04	Ois	4580	8130	1.660	0.315	0.581	0.067	419	52	44	11	yes	–	24.4 ± 1.7 (ZHe, ECO04)
	CSM05	Csa	5220	9060	–	–	–	–		–	–	–	yes	yes	34.9 ± 5.5 (ZHe, ECO05)
	CSM02	Csa	5900	9690	1.424	0.111	0.701	0.015	282	10	42	6	yes	–	39.2 ± 5.5 (ZHe, ECO02)
	RA14–70	Sks	3360	2800	0.871	0.048	0.677	0.018	233	21	30	13	yes	–	175.6 ± 91.0 (ZHe, ECO-IAZ02)
	RA14–448	Dic	1420	1000	1.173	0.343	0.661	0.047	288	35	34	13	–	–	318.1 ± 20.7 (ZHe, ECO-IAZ04), 272.4 ± 22.6 (ZHe, ECO-IAZ05)
	RA14–85	Opi	1860	6220	1.721	0.150	0.755	0.015	243	12	29	13	yes	–	
	RA14–396	Opi	1700	6250	1.577	0.410	0.757	0.037	221	30	34	12	yes	–	
	RA14–41	Ois	4700	8440	–	–	–	–	–	–	–	–	yes	–	
	RA14–39	Csa	5200	8750	–	–	–	–	–	–	–	–	yes	yes	
	RA14–93	Cth	7340	12,290	–	–	–	–	–	–	–	–	yes	yes	35.1 ± 2.7 (ZHe, ECO93), 136.8 ± 7.1 (ZFT, ECO93)
Central EC	RA14–185	Oob	3440	11,250	1.892	0.221	0.760	0.022	241	18	27	15	yes	–	
	RA14–296	Ojc	640	9060	2.340	0.202	0.737	0.021	257	31	33	13	yes	–	
	RA14–199	Opt	1100	7500	2.369	0.423	0.755	0.054	225	51	54	7	yes	–	
	RA14–162	Oat	2660	11,250	1.910	0.383	0.627	0.029	375	41	39	11	yes	–	
	CGO21	Oob	1840	9000	1.848	0.083	0.685	0.026	323	28	36	10	yes	–	26.6 ± 1.4 (ZHe, ECO21)
	CGO22	Oci	2100	10,000	0.913	1.080	0.461	0.097	377	49	44	10	yes	yes	346.5 ± 21.6 (ZHe, ECO22)
	RA14–146	Opi	1820	8440	3.082	0.859	0.551	0.064	313	194	126	10	yes	–	
	CGO23	Oat	1400	8750	0.824	0.147	0.514	0.023	397	16	32	11	yes	–	
	CGO24	Oci	2180	10,000	1.924	0.786	0.736	0.023	221	33	40	9	yes	yes	268.6 ± 86.7 (ZHe, ECO24)
	RA14–136	Opi	600	7190	3.380	0.588	0.534	0.040	303	160	90	14	yes	–	
	RA14–128	Oob	1840	9060	2.636	0.858	0.417	0.070	519	139	79	14	yes	–	
Western EC	RA14–293	Omq	5220	10,060	1.844	0.512	0.640	0.063	352	35	34	13	yes	yes	179.5 ± 112.6 (ZHe, ECO293)
	RA14–284	Oag	3100	7880	2.534	0.267	0.709	0.009	271	23	33	11	yes	–	
	RA14–280	Oko	1880	6640	2.135	0.234	0.730	0.005	271	8	27	14	yes	–	
	RA14–261	Oag	2740	6880	2.743	0.305	0.663	0.010	296	36	71	3	yes	yes	
	RA14–248	Omq	3620	8130	2.479	0.182	0.527	0.037	472	44	39	12	yes	yes	
	RA14–241	Oag	340	6880	2.664	0.412	0.677	0.030	284	21	30	13	yes	yes	

Note: R1, R2, and peak temperature values calculated using the calibration of Rahl et al. (2005). Internal variability in R1, R2, and peak temperature is indicated by 1σ uncertainty. Temperature is also reported with 2 standard errors (SE), calculated after Cooper et al. (2013), from quadratic addition of 1σ internal error and external error of ±50 °C from the Rahl et al. (2005) calibration, divided by the square root of the number of analyses (n). Stratigraphic depths calculated below estimated Late Cretaceous and late Paleozoic paleo-surface from Fig. 4B and C. All samples were collected from shale or intercalated shale layers within quartzite. Map unit abbreviations: Dic- Devonian Icla Fm., Sks- Silurian Kirusillas Fm., Oko- Late Ordovician Kollpani Fm., Oag- Late Ordovician Angosto Fm., Omq- Late Ordovician Marquina Fm., Ojc- Middle Ordovician Potero Fm., Ose- Early Ordovician Sella/Pircancha Fm., Opi- Early Ordovician Pircancha Fm., Oat- Early Ordovician Agua y Toro Fm., Oob- Early Ordovician Obispo Fm., Oci- Early Ordovician Cieneguillas Fm., Ois- Early Ordovician Iscayachi Fm., Csa- Cambrian Sama Fm., Cth- Cambrian Torohuayco Fm.

Paleozoic rocks in the EC (Fig. 8). The IC temperatures closely match the RSCM temperatures from similar stratigraphic levels, and the IC and RSCM temperature estimates generally overlap within error with the estimated range of quartz recrystallization deformation temperatures. Though quartz microstructures structures provide a rough temperature estimation, this consistency suggest that the rocks were deformed at or near peak temperatures during the same low-grade metamorphic event (e.g., Law, 2014; Long et al., 2016). Given their agreement, we discuss below the three temperature datasets together to explore the timing of peak temperatures in the EC, the Paleozoic geothermal gradient, and the time-space pattern of pre-Andean exhumation.

5.1. Timing of peak metamorphism and late paleozoic exhumation

Combined zircon (U—Th)/He (ZHe), zircon fission track (ZFT), and illite/white mica K—Ar systems can elucidate the timing and rates of cooling through a closure temperature range of ~310 to ~180 °C (Reiners et al., 2005; Bernet, 2009; Harrison et al., 2009). Here, we utilize published ZHe and ZFT (Anderson et al., 2018) and illite K—Ar ages (Jacobshagen et al., 2002) in southern Bolivia to better understand the timing of attainment of peak temperature conditions. Additionally, the relationship between depth and sample cooling ages is used to evaluate the thermal structure and exhumation history of the upper crust (e.g., Gleadow et al., 1986; Stockli, 2005).

For the ZHe system, the partial retention zone (PRZ) occurs at temperatures of ~130–200 °C, but for typical orogenic cooling rates of ~10 °C/Myr the closure temperature has been shown to be ~180 ± 10 °C (Guenthner et al., 2013; Reiners et al., 2004). For the ZFT system, lab experiments indicate that the partial annealing zone (PAZ) spans temperatures of ~262–330 °C (Yamada et al., 2007), but field-based studies estimate a closure temperature closer to ~240 ± 10 °C, assuming orogenic cooling rates of ~10 °C/Myr (Bernet, 2009; Brandon et al., 1998).

K—Ar and $^{40}Ar/^{39}Ar$ step-heating data from micron- to submicron-scale illite grains has commonly been used to date low-grade regional metamorphism (e.g., Hunziker et al., 1986; Jaboyedoff and Cosca, 1999; Wyld et al., 2003), but more recent studies emphasize its utility as a low-temperature thermochronometer (e.g., Haines and van der Pluijm, 2008; Rahl et al., 2011; Verdel et al., 2012; Clauer, 2013; Süssenberger et al., 2018). Though there are no experimentally based Ar diffusion parameters for illite, theoretical predictions based on muscovite diffusion parameters indicate an effective closure temperature of 250–310 °C for fine-grained illite with diffusion radii of 0.1–1.0 μm and cooling rates of 1–10 °C/Myr (Harrison et al., 2009; Rahl et al., 2011). This is consistent with field-based studies that indicate complete

resetting of the illite/muscovite Ar thermochronometer for the <2 μm size fraction in a regional metamorphic setting at ~300 °C (Verdel et al., 2012). The important observation is that the closure temperature and apparent partial retention zone of the illite/muscovite Ar thermochronometer overlaps with the experimental ZFT PAZ at ~262–330 °C (Yamada et al., 2007; Verdel et al., 2012; Süssenberger et al., 2018). We note that the K—Ar ages reported in Jacobshagen et al. (2002) are limited by the uncertainties regarding excess Ar or Ar loss. However, K—Ar dating of fine-grained minerals has an advantage when compared with $^{40}Ar/^{39}Ar$; since it does not require irradiation, it avoids problems such as ^{39}Ar, necessary encapsulation, and reintegration of recoiled ^{39}Ar (e.g, Clauer, 2013). Therefore, we use these data to simply provide a broad timeframe for cooling through temperatures between ~310 and ~ 250 °C.

ZFT ages from the deepest units in the regional transect show that Paleozoic rocks did not experience temperatures above ~240–260 °C since the Late Jurassic-Early Cretaceous (~147–137 Ma, Anderson et al., 2018). This demonstrates that the peak and deformation temperatures recorded in the samples are definitively from a pre-Andean event and are not related to heating during Cenozoic synorogenic burial (Fig. 9A). Although deformation and attainment of peak temperatures could still be attributed to one of several Paleozoic tectonic events that affected the western margin of South America during construction of the Terra Australis Orogen (e.g., McGroder et al., 2015), or even early to middle Mesozoic continental rifting in the region (e.g., Mon and Salfity, 1995; Sempere et al., 2002), the K—Ar and ZHe ages in the Ordovician rocks indicate late Carboniferous (~320–280 Ma) metamorphism and deformation during the Gondwanide Orogeny (Fig. 9A; Jacobshagen et al., 2002; Anderson et al., 2018). In light of new constraints on the illite K—Ar closure temperature (e.g., Verdel et al., 2012), we interpret that the illite K—Ar ages across the EC most likely reflect erosional exhumation at or near the time when rocks cooled from peak temperature conditions. In general, illite K—Ar ages show that Ordovician rocks were thermally reset after deposition and accompanying sedimentary burial, and then subsequently cooled below ~310 °C (upper limit of closure of the <2 μm size fraction) at ~374–312 Ma, and below ~250 °C (closure of the <0.2 μm size fraction) around ~324 and 277 Ma (Fig. 9B). Anomalously young K—Ar ages (~250–133 Ma) are localized along the axis of the Mesozoic rift zone near the village of Tupiza (e.g., Sempere et al., 2002), and likely reflect thermal perturbation related to Mesozoic extension that have not affected all samples (Jacobshagen et al., 2002).

This interpretation is consistent with our RSCM data from samples directly below the unconformity, which would require ~5–12 km of pre-Cretaceous overburden (assuming a range of geothermal gradients between 20 and 50 °C/km; e.g., Fig. 8) in order to attain peak temperatures of ~250–300 °C (Supplementary Fig. 1A). ZHe data from Ordovician-Devonian rocks across the EC and the EC-IAZ boundary show that samples cooled below ~180 °C between the early Carboniferous and early Miocene (Anderson et al., 2018) (Fig. 9A-B). However, considering the distribution of all individual ZHe grain ages from these samples ($n = 110$), a distinct peak supported by 27 grains is centered at 291 ± 5 Ma (Fig. 9C), which illustrates that samples from Ordovician-Devonian rocks were thermally reset via subsidence and stratigraphic burial prior to the Late Carboniferous, and then cooled through ZHe closure during exhumation by Late Carboniferous time. The younger ZHe age peaks can be interpreted either as samples that

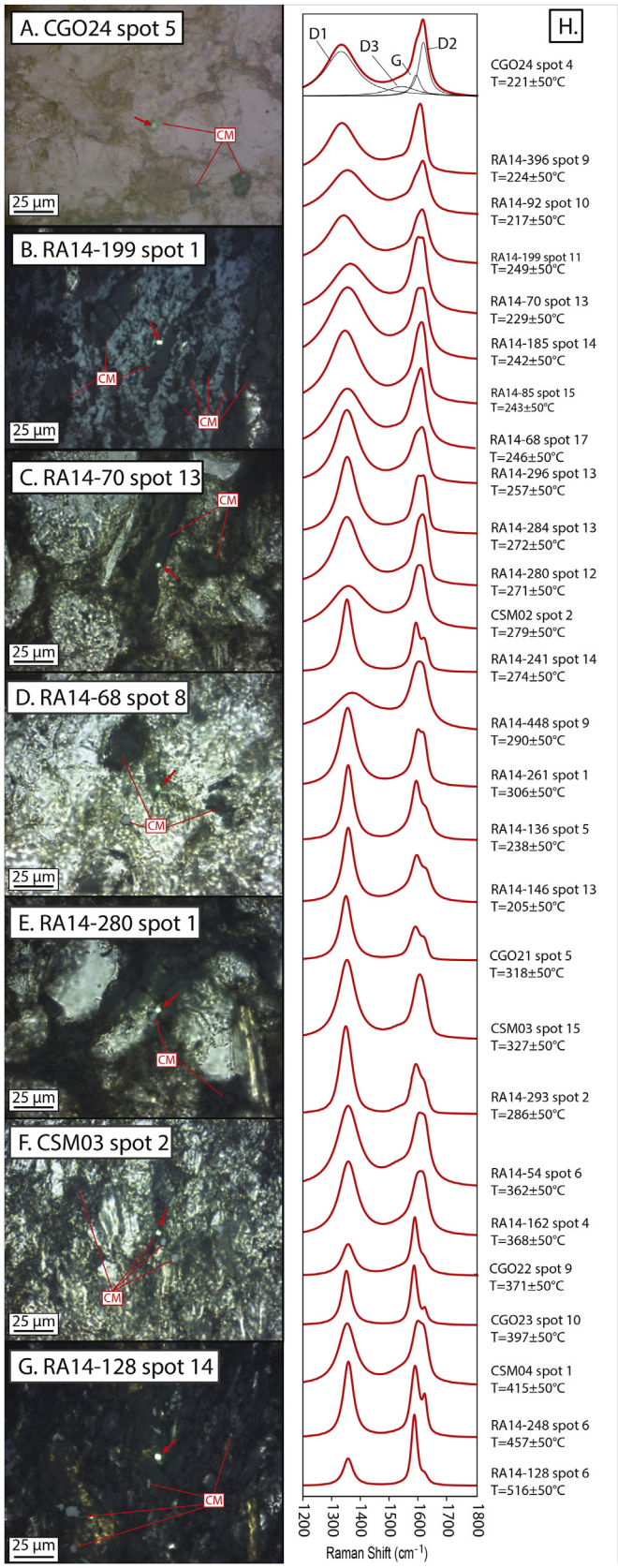

Fig. 7. A-G) Photomicrographs (plane polarized light) illustrating representative examples of analyzed carbonaceous material (CM). Green spot in the photos is the Raman laser beam. H). Examples of representative Raman spectra from each of the 27 samples analyzed for RSCM thermometry. All individual spots are shown with a 50 °C error after the Rahl et al. (2005) calibration. The positions of the graphite (G) and defect (D1, D2, D3) peaks are shown in black for the top spectrum. Peak temperatures (T) and R1 and R2 parameters were calculated after Rahl et al. (2005). Spectra are arranged in order from low to high temperature. See Supporting Information for peak center positions, heights, amplitudes, and areas for individual spot analyses. (For interpretation of the references to color in this figure legend, the reader is referred to the web version of this article.)

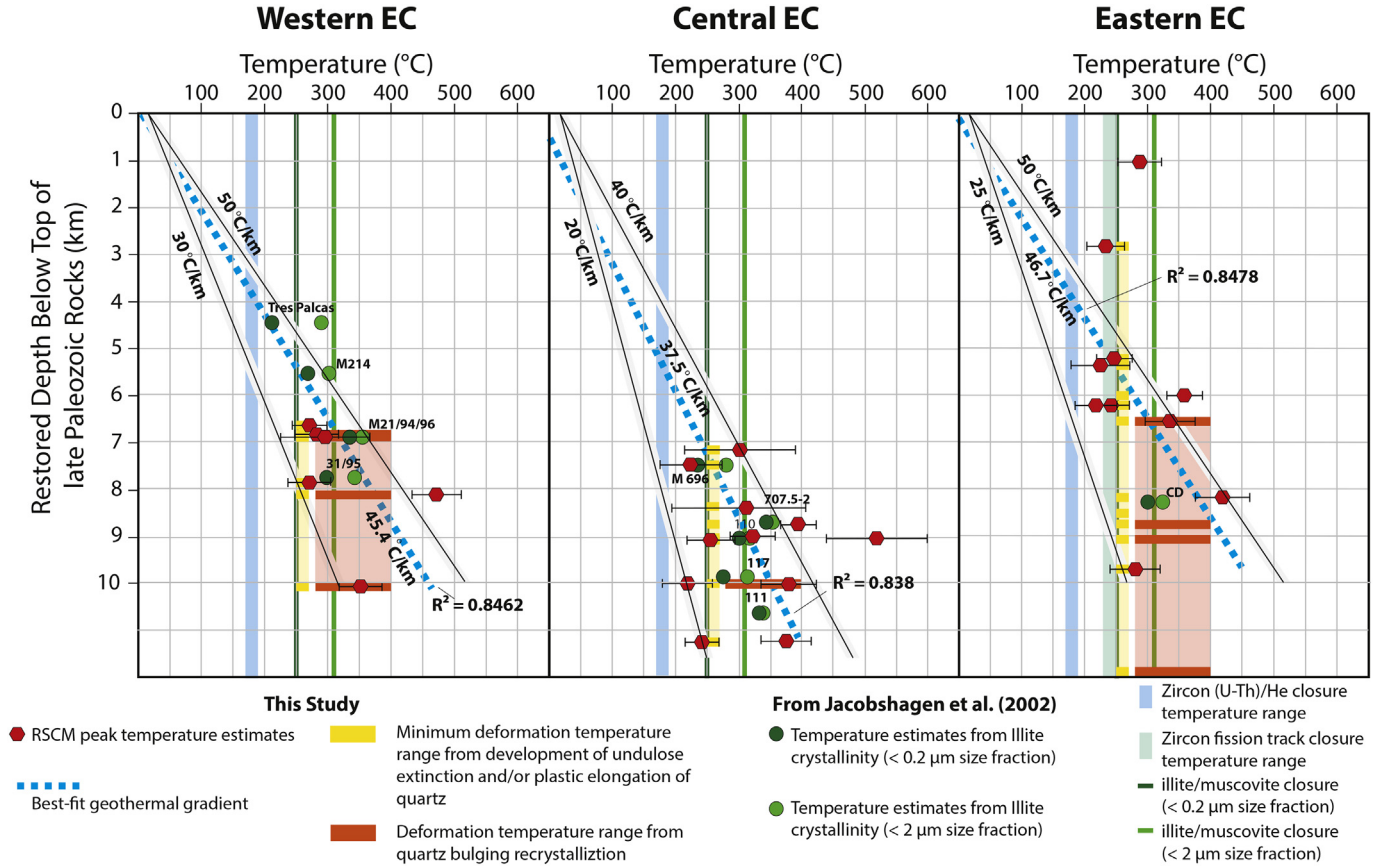

Fig. 8. Graphs of peak temperature versus stratigraphic depth below the late Paleozoic paleo-surface level from the Paleozoic reconstruction in Fig. 5C for the 31 analyzed samples, and compiled illite crystallinity data from Jacobshagen et al. (2002). Vertical bars denote closure temperature ranges for low-temperature thermochronometers.

Table 2
Illite crystallinity data and K—Ar ages compiled from Jacobshagen et al. (2002).

Sample	IC value (Δ°2Θ)		Temperature (°C)		K-Ar age ± 2σ (Ma)		Restored Structural Depth (m)		Metamorphic Zone
	(<2 μm)	(<0.2 μm)	(<2 μm)	(<0.2 μm)	(<2 μm)	(<0.2 μm)	K.	Pz.	
31/95	0.180	0.240	342	299	347.1 ± 7.3	287.7 ± 7.8	3500	7500	epizone-anchizone
M214	0.238	0.300	301	266	374.8 ± 8.0	324.5 ± 6.9	1600	5530	epizone-anchizone
Tres Palcas	0.260	0.435	287	211	365.1 ± 7.5	311.5 ± 7.0	200	4445	anchizone
M 21/94/96	0.165	0.190	355	334	137.1 ± 3.2	133.2 ± 4.5	1200	6910	epizone
M 707.5–2	0.170	0.180	351	342	223.4 ± 4.7	203.2 ± 4.8	3750	8710	epizone
M 696	0.275	0.350	279	243	251.7 ± 6.5	191.5 ± 4.1	2900	7770	anchizone
117	0.220	0.285	312	274	334.6 ± 7.2	296.4 ± 7.4	1450	9830	epizone-anchizone
111	0.190	0.195	334	330	312.2 ± 7.0	289.8 ± 6.2	3200	10,665	epizone
110	0.215	0.240	316	299	323.1 ± 6.7	288 ± 5.9	2200	9000	epizone-anchizone
CD	0.205	0.235	323	302	312.4 ± 7.0	276.9 ± 7.3	3200	8265	epizone

Note: Illite crystallinity values converted to temperature using the relationship T(°C) = −148.95 × ln (IC value) + 86.77 from Zhu et al. (2016). IC values are determined by measuring the width of the basal 1-nm illite XRD peak at one-half of its height, reported in units of Δ°2Θ where°2Θ is the XRD angle (Kübler, 1967; Kübler and Jaboyedoff, 2000). Samples are divided into two size fractions: <2 μm and < 0.2 μm. The diagenetic zone (zeolite facies) is defined as IC >1°2Θ, the deep diagenetic zone is defined as IC between 0.42° and 1°2Θ, the low anchizone (prehnite-pumpellyite facies) is defined as IC between 0.30° and 42°2Θ, high anchizone is defined as IC as 0.25° to 30°2Θ, and epizone (lower greenschist facies) is defined as IC < 25°2Θ (Merriman and Peacor, 1999).

resided in the ZHe PRZ, were thermally reset during subsequent synorogenic burial and then later exhumed during Cenozoic orogenesis, or were affected by radiation damage that resulted in reduced He retention and anomalously young ages (Anderson et al., 2018). For Ordovician samples ($n = 5$) from ~3 km below the unconformity, which reached RSCM peak temperatures of ~250–300 °C, ZHe ages show that these samples cooled below ~180 °C in the Carboniferous-Early Permian (262–346 Ma) and likely did not achieve temperatures within the ZHe partial retention zone (~130–200 °C) thereafter (Anderson et al., 2018). This is compatible with the illite K—Ar ages that encompass the same stratigraphic levels, which show an earlier (or partially overlapping) period of cooling from near-peak temperatures (~310–250 °C) at ~374 to 277 Ma.

Age-depth analysis evaluates the apparent age pattern of thermochronologic data as a function of paleodepth, by utilizing the concept of exhumed fossil partial retention and partial annealing zones to contextualize cooling data (e.g., Gleadow et al., 1986; Stockli, 2005). Age-depth analysis can provide context for interpreting the cooling ages discussed above, particularly the illite K—Ar ages. Anderson et al. (2018) documented a fossil ZHe PRZ exposed across the Cuesta de Sama anticlinorium, which we utilize here to elucidate the pre-Cenozoic thermal structure of the crust and earlier periods of rapid cooling.

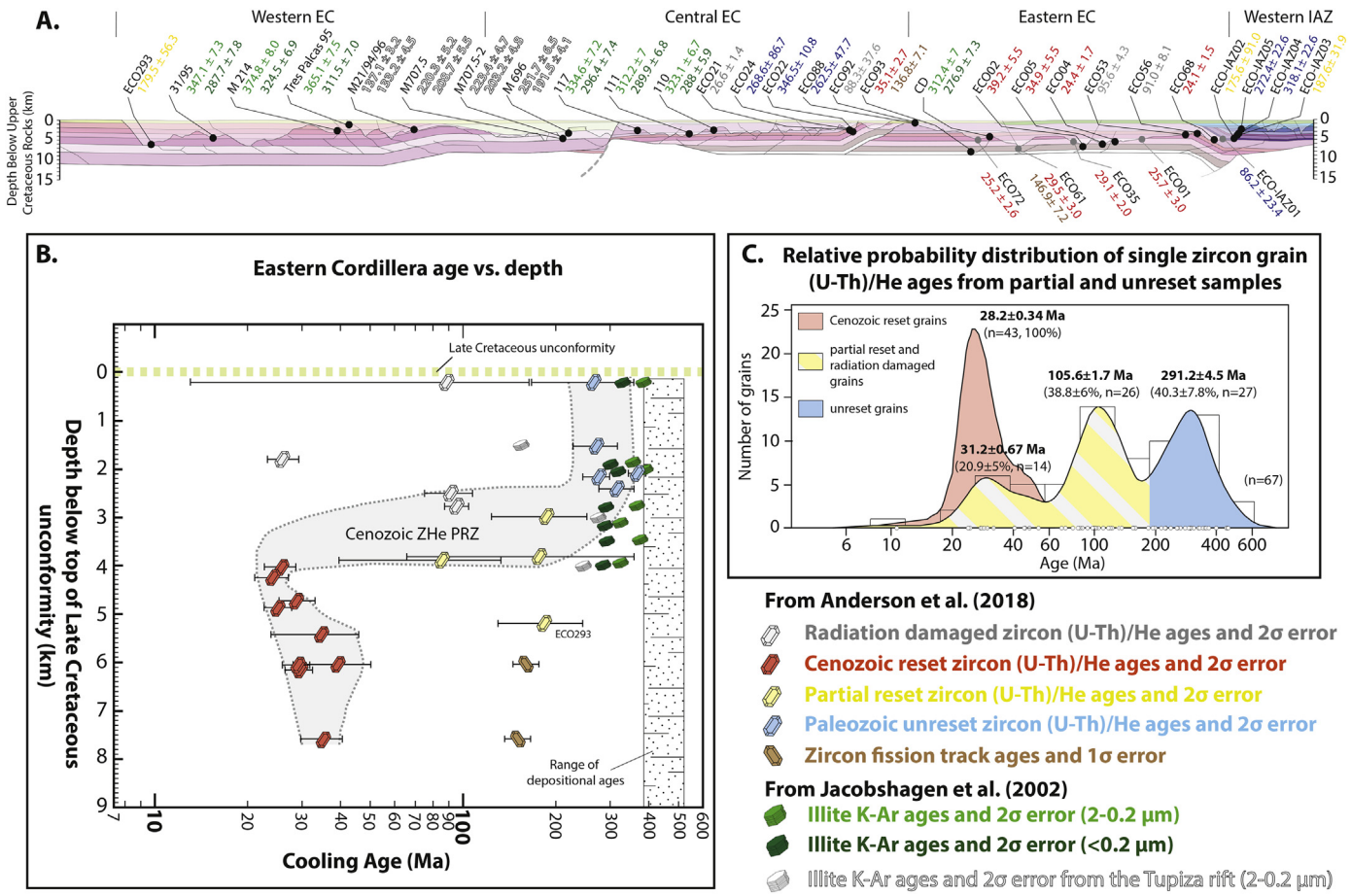

Fig. 9. Zircon (U—Th)/He, zircon fission track, and illite K—Ar data from across the Eastern Cordillera. A) Low-temperature cooling ages projected to the restored cross-section configuration at the end of the Late Cretaceous. Text color corresponds to dating techniques from Anderson et al. (2018) and Jacobshagen et al. (2002) shown at the bottom of the fig. B) Age-depth profile of low-temperature cooling ages relative to the base-Cretaceous unconformity (modified from Anderson et al., 2018). For a non-log plot showing ages >100 Ma, see Supplementary Fig. 2. C) Relative probability plot of all zircon (U—Th)/He single grain ages ($n = 110$) across the EC from Anderson et al. (2018).

On Fig. 9B, all ZHe and ZFT ages (Anderson et al., 2018) and illite K—Ar ages (Jacobshagen et al., 2002) are plotted as a function of depth relative to the base-Cretaceous unconformity. At depths < ~3 km below the unconformity, ZHe ages from Ordovician-Devonian rocks display an age-depth relationship that is younger than the depositional age of Devonian strata (~400–380 Ma; Troth et al., 2010). This implies that after Late Devonian time, these samples were buried to temperatures above the total ZHe diffusion isotherm (~200 °C) and were thermally reset before rapid exhumation through ZHe closure. However, the fossil ZHe PRZ as it is observed today developed during subsequent static thermal conditions that persisted until rapid Cenozoic exhumation (Anderson et al., 2018). Therefore, only the upper part of the ZHe age-depth profile preserves a record of this late Paleozoic exhumation event because samples at depths >3 km were later fully or partially reset. We interpret the ~345–270 Ma age range of the upper inflection point on the Cenozoic fossil ZHe PRZ profile to reflect the late Paleozoic onset of rapid cooling through ZHe closure (Fig. 9B). This is consistent with the ~291 ± 5 Ma ZHe age peak defined by the distribution of all single grain cooling ages (Fig. 9C). After ~270–300 Ma, samples < ~3 km below the unconformity never attained temperatures > ~130 °C.

The age-depth patterns of the illite K—Ar ages indicate that samples spanning up to ~4 km below the Cretaceous unconformity were likely exhumed from depths below the base of the illite/muscovite Ar PRZ for the <0.2 μm size fraction (> ~ 250 °C), but were possibly within or just below the lower part of the PRZ for the <2 μm size fraction (~310 °C) (Fig. 9B). The <2 μm size fraction ages from Ordovician rocks show a steeply inclined age-depth pattern that gets older with decreasing depth, approaching the depositional age of the Devonian Huamampampa Formation (~388–392 Ma, Troth et al., 2010). This trend indicates that shallower samples likely resided within the lower part of the illite K—Ar PRZ and may explain why the <2 μm size fraction ages in samples M 214 and Tres Palcas are ~20–30 Myr older than all other ages (Table 2, Fig. 9A). Accordingly, IC values from these samples suggest temperatures of 266–301 °C and 211–287 °C (Table 2). The maximum timing for onset of rapid cooling through 2 μm illite K—Ar closure (~310 °C) is limited by the oldest observed age (~374 Ma). However, we interpret a younger onset of ~347–310 Ma to be more likely, as this age range is defined by 5 samples below the subtle inflection point ~2 km below the base-Cretaceous unconformity (Fig. 9B). The ages from the <0.2 μm size fraction are grouped in a tight cluster that define rapid cooling from temperatures >250 °C in a narrow ~310–290 Ma timeframe.

Though there are not enough samples to define a full ZFT age-depth profile, the two ZFT samples collected at this latitude have homogeneous individual grain age distributions that show a later period of rapid cooling through ZFT closure (~240 ± 10 °C) in the Late Jurassic-Early Cretaceous (Anderson et al., 2018). Because there are no illite K—Ar ages from deeper rocks, the thermal history prior to ~147–137 Ma is less certain for depths >4 km below the Cretaceous unconformity. However, given that the ZFT and the <0.2 μm illite/muscovite Ar systems share similar closure temperatures (~250–230 °C), we group the ZFT and < 0.2 μm illite K—Ar ages together into a combined age-depth profile that provides some insight. From this profile, we

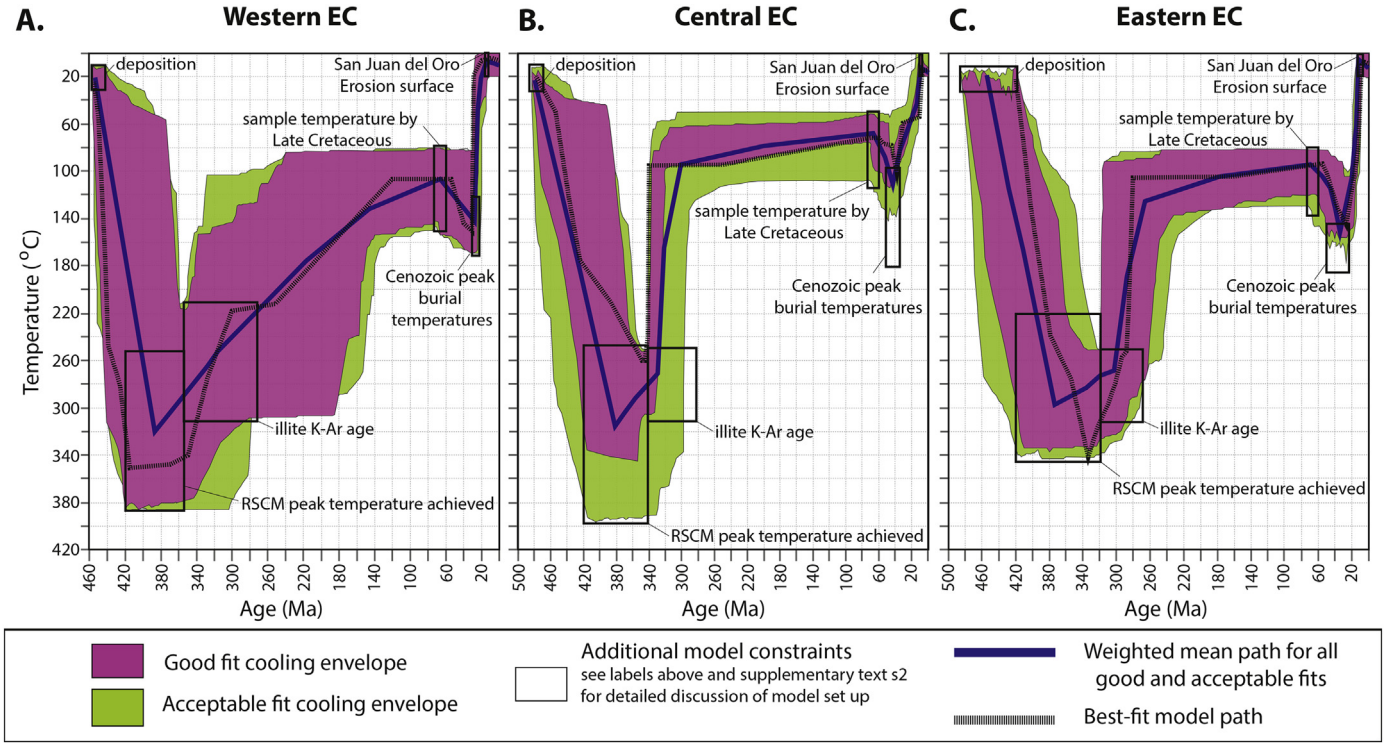

Fig. 10. Inverse models of t-T cooling envelopes (modeled in HeFTy; Ketcham, 2005) for composite samples in the Western (A), Central (B) and Eastern EC (C). For details of composite sample information and time-temperature path model parameter setup see supplementary information.

interpret the age offset between ZFT and < 0.2 μm illite K—Ar ages at ~4–6 km below the base-Cretaceous unconformity to define a composite PAZ-PRZ profile (Supplementary Fig. 2) that developed after Late Carboniferous-Early Permian cooling, and was later fossilized during Late Jurassic cooling. It is unclear if rocks at depths below ~6 km remained at elevated temperatures above ~230–250 °C after late Paleozoic cooling or if they were subjected to cooling and subsequent reheating in the Mesozoic. However, the timing of Late Jurassic-Early Cretaceous cooling does coincide with the timing of elevated crustal temperatures related to development of the Salta Rift in NW Argentina (Salfity and Marquillas, 1994; Lucassen et al., 1999) as well as the youngest illite K—Ar age within the Tupiza rift region. Except within close proximity to the Tupiza Rift (e.g., Jacobshagen et al., 2002), Ordovician rocks at depths <~6 km below the unconformity were never at temperatures > ~250–310 °C after ~347–290 Ma. At deeper stratigraphic levels (>6 km), rocks cooled below the ZFT closure temperature much later, but never reached temperatures greater than ~230–250 °C after ~136 Ma.

To summarize, Paleozoic rocks in the EC attained peak temperatures of ~220 to ~400 °C prior to removal of at least ~5 km of overburden, which resulted in cooling from ~310 to ~180 °C between ~347 and ~ 270 Ma. Development of vertical cleavage and recrystallization of quartz at near-peak temperatures demonstrate that the Paleozoic rocks were subjected to horizontal compression prior to Carboniferous exhumation (Kley et al., 1997). Our Paleozoic cross-section reconstruction can account for this missing overburden as Ordovician-Devonian sedimentary rocks that have been eroded away. Retro-deforming the monoclinal structures at the EC-IAZ boundary and in the western EC (Fig. 5C, annotations 5) restores the necessary missing overburden (>5 km) and implies that activation of these first-order structures was the primary mechanism for initiating late Paleozoic exhumation, though regional uplift could be associated with possible uncharacterized deeper structures as well. Very little shortening (a minimum of ~13 km) was accommodated in the EC by first order structures during this event compared to Cenozoic deformation (~120 km) (compare length in Fig. 5A-C). However, 13 km of shortening should be considered a minimum, as it does not include penetrative strain accommodated by bedding-normal cleavage development, which may require ~15–20% shortening. Given that stratigraphic burial was the most likely mechanism for samples to achieve peak temperature, depositional constraints on the Devonian Huamampampa Formation (e.g., Troth et al., 2010) place an important limit on the time at which peak temperatures were attained. Palynological data indicate a depositional age of ~388–392 Ma for this unit (Fig. 3; Troth et al., 2010), and ZHe data show that the Huamampampa Formation at the EC-IAZ boundary was thermally reset by 272.4 ± 22.6 Ma (Fig. 9A; Anderson et al., 2018). Thus, peak temperatures in the underlying rocks at the EC-IAZ boundary had to have been attained after 388 Ma, but before ZHe cooling at 310–270 Ma. Given that Devonian-Permian strata in the central Andes are interpreted to represent a foreland basin system that migrated eastward through time (e.g., Isaacson and Díaz Martínez, 1995; Calle et al., 2017), we assume that peak burial was older in the western EC, though probably no older than Devonian.

5.2. Metamorphic field gradients and implications for Paleozoic burial depths

Peak temperature measurements span a ~ 10 km thickness of Paleozoic rocks, which allows us to estimate upper-crustal temperature gradients in the EC. Because the samples span an east-west restored distance of ~300 km, they do not represent a true vertical column (Fig. 5C). Instead, the apparent thermal gradients are more appropriately considered a metamorphic field gradient rather than a true estimate of the peak geothermal gradient (e.g., Long and Soignard, 2016).

Calculation and interpretation of metamorphic field gradients in the EC relies on the assumption that the peak temperatures recorded in Paleozoic rocks are related to the same metamorphic event and were achieved at roughly the same time, and that our Paleozoic

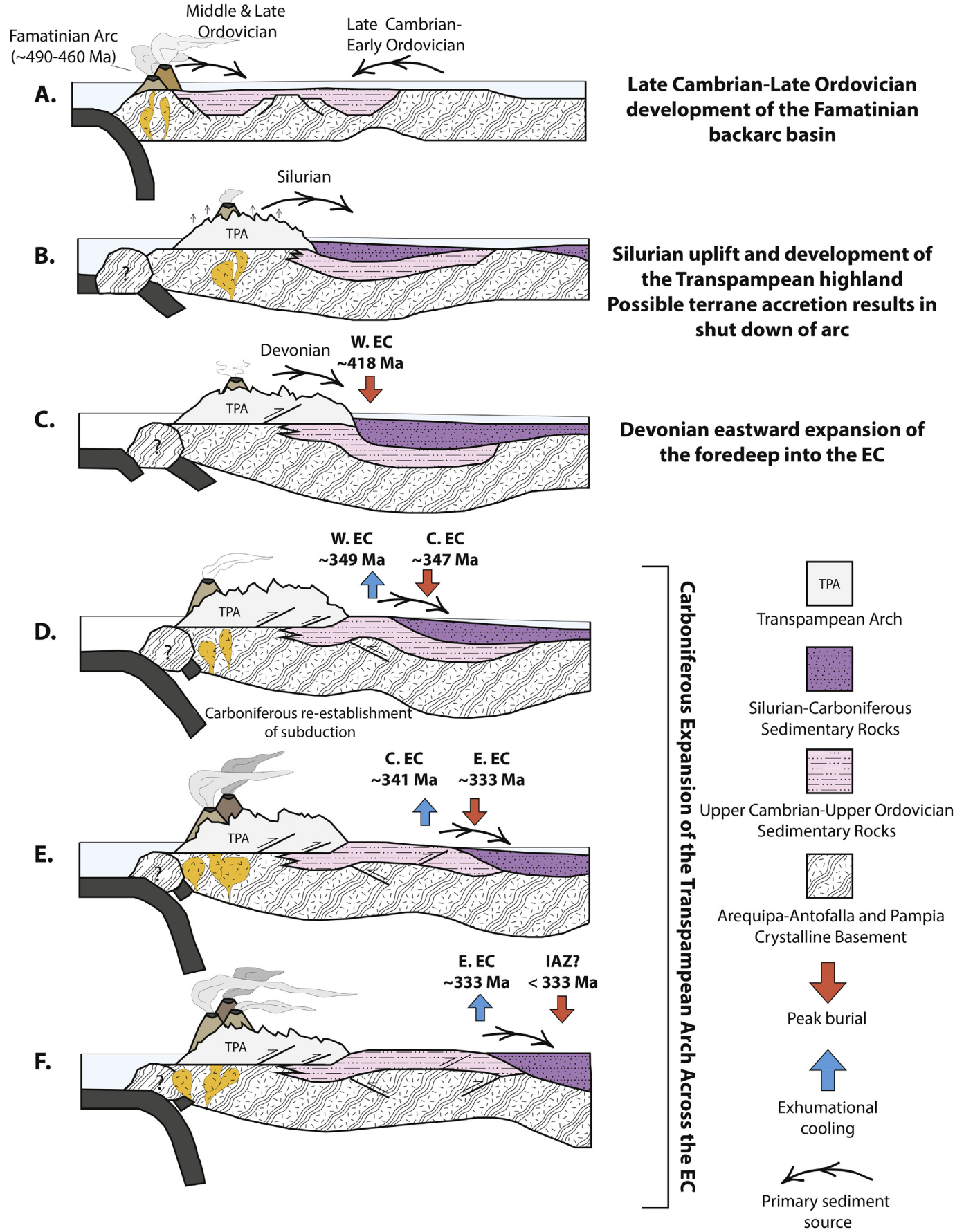
Famatinian Arc
(~490-460 Ma)
Middle & Late
Ordovician
Late Cambrian-
Early Ordovician
A.
Late Cambrian-Late Ordovician development of the Famatinian backarc basin
Silurian
TPA
B.
Silurian uplift and development of the Transpampean highland
Possible terrane accretion results in shut down of arc
Devonian
W. EC
~418 Ma
TPA
C.
Devonian eastward expansion of the foredeep into the EC
W. EC
~349 Ma
C. EC
~347 Ma
TPA
D.
Carboniferous re-establishment
of subduction
C. EC
~341 Ma
E. EC
~333 Ma
TPA
E.
E. EC
~333 Ma
IAZ?
< 333 Ma
TPA
F.
Carboniferous Expansion of the Transpampean Arch Across the EC
TPA
Transpampean Arch
Silurian-Carboniferous
Sedimentary Rocks
Upper Cambrian-Upper Ordovician
Sedimentary Rocks
Arequipa-Antofalla and Pampia
Crystalline Basement
Peak burial
Exhumational
cooling
Primary sediment
source

reconstruction (Fig. 5C) provides a reasonable estimate of original stratigraphic or structural burial depth of samples. The preceding discussions argue that this is the case. We assume a surface temperature of 15 ± 10 °C and assume that the surface level during peak metamorphism was likely at the top of the Devonian or Carboniferous section interpreted from our Paleozoic structural reconstruction.

Given the broad across-strike distance of the samples, peak temperature data were sorted into the western, central, and eastern EC and obvious outliers (e.g., RA14–128, RA14–448, CSM02) were not included in the calculation of metamorphic field gradients for each zone. Best-fit lines yield relatively good fits to the data (~R^2 = 0.84–0.85) and define metamorphic field gradients of 45 °C/km in the western EC, 38 °C/km in the central EC, and 47 °C/km in the eastern EC (Fig. 8). The intercepts from the best-fit lines predict Paleozoic burial depths that closely match the Paleozoic cross-section reconstruction, and these metamorphic field gradients are consistent with the pre-Late Cretaceous paleogeothermal gradients implied from an interpreted isotherm at the base of the PAZ/PRZ on the composite ZFT – illite K—Ar age-depth profile (~40 °C/km). While these metamorphic field gradients are relatively elevated, we note that back-arcs within accretionary orogens are always regions of high heat flow (Cawood et al., 2009).

5.3. Thermal modeling insights into time-space patterns of peak temperature and exhumation

Sample data that best represent the western, central, and eastern EC were inverse modeled to provide more quantitative estimates of the full thermal history and onset of rapid exhumation related to orogenesis in each zone. We used the program HeFTy (Ketcham, 2005), which employs a Monte Carlo approach to generate a large number of time-temperature (t-T) cooling paths from which thermochronologic data are predicted according to published FT annealing and He diffusion models (see supplementary information for detailed methods and model parameters). The resulting predicted data for each t-T path are compared to the measured cooling ages of each individual sample and reported as envelopes classified as good (0.5) or acceptable (0.05) using a probability of fit calculated with a Kuiper's statistical test (Ketcham, 2005). We manually imposed additional model constraints such as depositional age from published fossil or palynological data for Paleozoic units, peak temperature conditions from our RSCM data, and the limit of cooling through ~250–310 °C from the K—Ar illite ages. Cenozoic peak burial constraints are also included in the models, after Anderson et al. (2018). We note that no single sample has a full suite of thermochronologic, peak temperature, or depositional age data, so the thermal models are built from a composite of adjacent samples from similar stratigraphic levels. As such, the models are a generalization of the thermal history of the western, central, and eastern EC.

In the western EC, we modeled a composite of samples that includes cooling ages from samples ECO293 (Anderson et al., 2018) and 31/95 (Jacobshagen et al., 2002), and RSCM temperatures from RA14–284 and RA14–293 (Fig. 10A). Good fit *t-T* paths define attainment of peak temperatures as high as ~380 °C between ~420 and 341 Ma, followed by cooling at moderate rates (~2–6 °C/Myr) beginning at ~352–341 Ma. Cooling was slow thereafter (~1 °C/Myr or less) until Cenozoic reburial and exhumation, except for a possible moderate (~4 °C/Myr) cooling event at ~160–130 Ma.

In the central EC, we modeled cooling age data from samples ECO22 (Anderson et al., 2018), 110, 111, and 117 (Jacobshagen et al., 2002), and the mean RSCM temperature (322 ± 75 °C) from samples CGO21, CGO22, CGO23, CGO24, RA14–146, RA14–162, and RA14–185 (Fig. 10B). Good fit *t-T* paths show attainment of peak temperatures of 346–251 °C between ~416 and 345 Ma, followed by rapid cooling (20 °C/Myr) beginning at ~354–332 Ma. Following rapid cooling, relatively low-temperature conditions (~60–100 °C) persisted until Cenozoic synorogenic burial beginning after ~60 Ma resulted in slightly elevated temperatures within the apatite partial annealing zone (~116–80 °C).

In the eastern EC, we modeled age data from samples ECO-IAZ03 (Anderson et al., 2018) and CD (Jacobshagen et al., 2002) and a mean RSCM temperature (282 ± 62 °C) from samples RA14–85, CSM03, RA14–54, RA14–68, RA14–396. Good fit t-T paths define attainment of peak temperatures of 331–252 °C between ~410 and 318 Ma, followed by rapid cooling (~4–6 °C/Myr) beginning at ~318–294 Ma. After this, temperatures remained static between ~135 and ~ 80 °C from ~245 Ma until Cenozoic burial and reheating to temperatures within the ZHe PRZ after ~60 Ma.

In summary, the thermal models define rapid cooling of the EC at ~352–294 Ma, which is consistent with the broad cooling age constraints (~347–270 Ma) discussed above. The models also illustrate that the timing of late Paleozoic peak burial and subsequent rapid cooling, which we interpret to be related to erosional exhumation during orogenesis, proceeded from west to east across the EC. This is evidenced by the best-fit path in each model; peak temperatures in the western EC were achieved after ~418 Ma and followed by rapid cooling at ~349 Ma, peak temperatures were achieved by ~347 Ma and followed by rapid cooling at ~341 Ma in the central EC, and peak temperatures were achieved by ~333 Ma and immediately followed by rapid cooling in the eastern EC.

5.4. Geodynamic implications: Foredeep migration and carboniferous eastward expansion of the transpampean arch

During and following the development of the Ordovician Famatinian-Western Puna Arc, sedimentary rocks in the EC were deposited in a back-arc basin setting (Fig. 11A; e.g., Coira et al., 1999; Astini and Dávila, 2004; Ramos, 2018). In southern Bolivia, the > ~12 km Cambrian-Ordovician section accumulated first by extensional fault-controlled subsidence, followed by establishment of a Middle to Late Ordovician foreland basin system (Egenhoff, 2007; Ramos, 2008; Calle et al., 2017). While contractional deformation and metamorphism associated with eastward expansion of deformation during the Late Ordovician-Silurian Ocloyic event is recorded in the Puna of NW Argentina (e.g., Coira et al., 1982; Mon and Hongn, 1991; Mon and Salfity, 1995), this tectonic event is not apparent in lower Paleozoic rocks in southern Bolivia (e.g., Jacobshagen et al., 2002). Based on quartz recrystallization microstructures, we interpret that Cambrian and Ordovician rocks were deformed at or near peak temperature conditions, which were attained after the end of the Silurian. Therefore, we propose that cleavage development was associated with the final construction of the Terra Australis Orogen and the incipient Gondwanide orogeny beginning in the Devonian or Early Carboniferous, rather than the Ordovician Ocloyic Orogeny. Previous authors attributed late Paleozoic deformation in southern Bolivia to the Hercynian or Chañic Orogenies (e.g., Starck, 1995; Tankard et al., 1995; Kley et al., 1997; Müller et al., 2002; Jacobshagen et al., 2002). Though timing for peak metamorphic conditions in the Devonian at this latitude are coeval with the Chañic orogeny, the Chañic belt is conventionally related a collisional orogeny limited to 28–38°S latitudes (Heredia et al., 2018). Further, the

Fig. 11. Schematic cross-section diagrams showing Paleozoic tectonic development along the western margin of Gondwana in southern Bolivian (~21°S) (modified from Calle et al., 2017). A. Early Cambrian-Late Ordovician development of the Famatinian backarc basin. B. Growth and uplift of the Transpampean Arch and Middle Silurian development of an integrated foreland basin system. C. Eastward expansion of the foredeep depocenter into the western EC by beginning of the Devonian. D—F. Carboniferous eastward migration of the foredeep depocenter and exhumation across the EC during expansion of the Transpampean Arch, based on timing constraints from the best-fit thermal models in Fig. 10. TPA = Transpampean Arch, W. EC = Western Eastern Cordillera, C. EC = Central Eastern Cordillera, E. EC = Eastern Eastern Cordillera.

Hercynian orogeny is more appropriately associated with closure of the Rheic Ocean, suturing of South American and Africa with North American and Europe, and development of the Variscan, Alleghanian, and Ouachita fold belts of Laurussia (e.g., Nance et al., 2010). Therefore, we favor the use of Gondwanide orogeny (e.g., Cawood, 2005; Heredia et al., 2018; Ramos, 2018) as the more appropriate term to describe late Paleozoic deformation in southern Bolivia.

Following the Ocloyic orogeny, contractional or transpressional deformation along the Gondwanan margin resulted in growth of the Transpampean orogenic highland (Tankard et al., 1995; McGroder et al., 2015). A pronounced lack of Middle Ordovician to Late Devonian zircons (~460–320 Ma) within Silurian and Devonian rocks in this region (~20° - 26°S) indicate cessation of magmatism during this time period (Einhorn et al., 2015; Calle et al., 2017; Koltonik et al., 2019). Lack of a volcanic arc along the western margin of Gondwana during the middle Paleozoic is more clearly linked with successive accretion and collision of allochthonous terranes (Cuyania and Chilenia) in central and southern Argentina and Chile (Ramos, 2008; Weinberg et al., 2018; Domeier and Torsvik, 2014; Einhorn et al., 2015; Oriolo et al., 2019). Whereas at ~21°S, extensive Neogene volcanic cover in the Coastal and Western Cordilleras obscures the Paleozoic plate margin history, and has led to an interpretation by some that the western margin of Gondwana at this latitude was passive during the Devonian (e.g., Bahlburg et al., 2009; Domeier and Torsvik, 2014). Nevertheless, sedimentary facies and provenance analysis of rocks in the IAZ, SAZ, and Chaco Plain indicate the development of a retroarc foreland basin system that migrated eastward from the Middle Silurian until the Late Carboniferous (Fig. 11B; Gohrbandt, 1993; Sempere, 1995; Isaacson, 1975; Isaacson et al., 1995; Isaacson and Díaz Martínez, 1995; McGroder et al., 2015; Calle et al., 2017; Koltonik et al., 2019). Though Silurian-Carboniferous rocks are missing in the EC, the RSCM temperatures, IC values, and metamorphic field gradients are consistent with removal of > ~ 5 km of overburden before development of the Mesozoic unconformity (e.g., Kley and Reinhardt, 1994; Jacobshagen et al., 2002). Our late Paleozoic cross-section configuration (Fig. 5C) illustrates that Silurian to Upper Devonian rocks preserved along the margins of the EC in the IAZ and Altiplano can account for this missing overburden, and provided the requisite burial depths to account for peak temperatures in Ordovician and Cambrian rocks. Our thermal models (Fig. 10) illustrate an eastward progression of peak temperature conditions that are followed by subsequent exhumation, which is consistent with the sedimentary record of an eastward-migrating foreland basin depocenter. We suggest that the attainment of peak temperatures occurred at peak burial, and therefore tracks the position of the foredeep depocenter (e.g., DeCelles and Giles, 1996) as it migrated eastward across the EC (Fig. 11C-F). The best-fit models show that this process occurred between ~418 and ~ 333 Ma (Fig. 10). Given these observations, it is likely that the western margin of Gondwana in southern Bolivia was an advancing accretionary orogen (e.g., Cawood et al., 2009) during the Devonian and perhaps part of the Silurian (Fig. 11B-C), though it is uncertain exactly what mechanism may have been responsible for orogen advance during this time frame (e.g., flat slab, terrane accretion).

The eastward progression of cooling across the EC is interpreted as the eastward advance of an eroding retroarc orogenic wedge during the Carboniferous Gondwanide orogeny. We interpret activation of the Paleozoic structures identified on Fig. 5C as one of the primary mechanisms that accommodated uplift and erosion of Silurian through Devonian-Lower Carboniferous rocks in the EC. However, development of pervasive, bedding-subnormal cleavage across the EC may have also contributed to additional east-west shortening, crustal thickening, and consequent uplift. The best-fit paths of the thermal models show that cooling initiated at ~349–333 Ma. From these timing constraints we estimate the rate of orogenic advance across the EC at 19 km/Myr. The rapid eastward expansion of exhumation across the EC coincided with a renewed input of magmatic zircons into the retroarc sedimentary basin in the present day IAZ and SAZ during the Carboniferous (Einhorn et al., 2015; Calle et al., 2017; Koltonik et al., 2019), which points to changing plate boundary conditions that favored reestablishment of subduction and the volcanic arc along the Gondwanan margin (Cawood, 2005; Bahlburg et al., 2009; Weinberg et al., 2018; Heredia et al., 2018). Plate kinematic models show rapid trench advance along the western Gondwana subduction zone and increased continental plate motion speeds in the period between 360 and 340 Ma (Domeier and Torsvik, 2014; Matthews et al., 2016), which may have promoted enhanced coupling and at the plate boundary that drove eastward advance of the orogenic wedge across the EC during the Carboniferous (e.g. Cawood et al., 2009). However, the onlap of Permian restricted marine rocks over a widespread region of western Gondwana signaled the end of contractional deformation in the central Andes until onset of Cenozoic Andean shortening (e.g., Sempere et al., 2002; McGroder et al., 2015).

6. Conclusions

Peak temperatures of Paleozoic rocks in the EC increase with depth, and range primarily between ~250 and ~ 400 °C. Peak temperatures overlap with deformation temperature ranges, suggesting that cleavage development and peak metamorphism in Ordovician rocks developed during the same orogenic event. Attainment of peak temperatures and subsequent exhumation progressed from west to east between ~420–318 Ma and ~ 352–294 Ma, respectively. The timing of peak temperature conditions reflects peak burial during eastward migration of a middle Paleozoic foredeep depocenter across the EC, and exhumation represents the eastward expansion of the Transpampean orogenic highland across the EC during the Carboniferous Gondwanide orogeny. Rapid eastward advance of the orogen coincided with changing subduction conditions along the Gondwanan margin.

Declaration of Competing Interest

The authors declare that they have no known competing financial interests or personal relationships that could have appeared to influence the work reported in this paper.

Acknowledgements

This work was funded by National Science Foundation grant EAR-1250510 awarded to Long and Horton. Additional funds for RSCM analyses were provided by the American Association of Petroleum Geologist Grants-in-Aid Program (Kenneth H. Crandall Memorial Grant) awarded to Anderson. Constructive reviews from Sebastian Oriolo and an anonymous reviewer greatly improved this manuscript. We thank Ramiro Matos for assistance with logistics, and Javier Matos for assistance in the field. We also thank Nick Perez and Tomas Capaldi, as well as conference and field trip attendees during the 11th South American Symposium on Isotope Geology (Bolivia, 2018) for valuable insight and discussions of pre-Andean geology. Thanks to Jesslyn Starnes for helpful advice for peak fitting RSCM data. All new data presented in this manuscript can be found in the accompanying supporting information files.

Appendix A. Supplementary data

Supplementary data to this article can be found online at https://doi.org/10.1016/j.gr.2021.03.002.

References

Allmendinger, R.W., Ramos, V.A., Jordan, T.E., Palma, M., Isacks, B.L., 1983. Paleogeography and Andean structural geometry, Northwest Argentina. Tectonics 2, 1–16. https://doi.org/10.1029/TC002i001p00001.

Allmendinger, R.W., Jordan, T.E., Kay, S.M., Isacks, B.L., 1997. Altiplano-Puna plateau of the Central Andes. Annu. Rev. Earth Planet. Sci. 25, 139–174. https://doi.org/10.1146/annurev.earth.25.1.139.

Anderson, R.B., Long, S.P., Horton, B.K., Calle, A.Z., Ramirez, V., 2017. Shortening and structural architecture of the Andean fold-thrust belt of southern Bolivia (21°S): implications for kine- matic development and crustal thickening of the Central Andes. Geosphere 13, 1–21. https://doi.org/10.1130/GES01433.1.

Anderson, R.B., Long, S.P., Horton, B.K., Thomson, S.N., Calle, A.Z., Stockli, D.F., 2018. Orogenic wedge evolution of the Central Andes, Bolivia (21°S): Implications for Cordilleran cyclicity. Tectonics 37. https://doi.org/10.1029/2018TC005132.

Arenas, R., Sanchez Martinez, S., 2015. Variscan ophiolites in NW Iberia: tracking lost Paleozoic oceans and the assembly of Pangea. Episodes 38, 315–333.

Arriagada, C., Roperch, P., Mpodozis, C., Cobbold, P.R., 2008. Paleogene building of the Bolivian Orocline: Tectonic restoration of the Central Andes in 2-D map view. Tectonics 27, TC6014. https://doi.org/10.1029/2008TC002269.

Astini, R.A., Dávila, F.M., 2004. Ordovician back arc foreland and Ocloyic thrust belt development on the western Gondwana margin as a response to Precordillera terrane accretion. Tectonics 23, TC4008. https://doi.org/10.1029/2003TC001620.

Bahlburg, H., Hervé, F., 1997. Geodynamic evolution and tectonostratigraphic terranes of northwestern Argentina and northern Chile. Geol. Soc. Am. Bull. 109, 869–884. https://doi.org/10.1130/0016-7606(1997)109<0869:GEATTO>2.3.CO;2.

Bahlburg, H., Breitkreuz, C., Zeil, W., 1987. Paleozoic basin development in northern Chile (21°–27°S). Geol. Rundsch. 76, 633–646. https://doi.org/10.1007/BF01821095.

Bahlburg, H., Vervoort, J.D., Andrew Du Frane, S., Bock, Barbara, Reimann, Cornelia, 2009. Timing of crust formation and recycling in accretionary orogens: Insights learned from the western margin of South America. Earth-Science Reviews 97 (1-4), 215–241. https://doi.org/10.1016/j.earscirev.2009.10.006.

Bailey, J.E., Hirsch, P.B., 1962. The recrystallization process in some polycrystalline metals. Proc. R. Soc. Lond. 267, 11–30.

Baludikay, B.K., François, C., Sforna, M.C., Beghin, J., Cornet, Y., Storme, J., Fagel, N., Fontaine, F., Littke, R., Baudet, D., Delvaux, D., Javaux, E.J., 2018. Raman microspectroscopy, bitumen reflectance and illite crystallinity scale: comparison of different geothermometry methods on fossiliferous Proterozoic sedimentary basins (DR Congo, Mauritania and Australia). Int. J. Coal Geol. 191, 80–94. https://doi.org/10.1016/j.coal.2018.03.007.

Bernet, M., 2009. A field-based estimate of the zircon fission-track closure temperature. Chem. Geol. 259 (3–4), 181–189. https://doi.org/10.1016/j.chemgeo.2008.10.043.

Bernet, M., Spiegel, C., 2004. Introduction: Detrital thermochronology. In: Bernet, M., Spiegel, C. (Eds.), Detrital Thermochronology—Provenance Analysis, Exhumation, and Landscape Evolution of Mountain Belts. 378. Geological Society of America Special Paper, pp. 1–6. https://doi.org/10.1130/0-8137-2378-7.1.

Beyssac, O., Goffe, B., Chopin, C., Rouzaud, J., 2002. Raman spectra of carbonaceous material in metasediments: a new geothermometer. J. Metamorph. Geol. 20, 859–871. https://doi.org/10.1046/j.1525-1314.2002.00408.x.

Beyssac, O., Goffe, B., Petitet, J.P., Froigneux, E., Moreau, M., Rouzaud, J.N., 2003. On the characterization of disordered and heterogeneous carbonaceous materials by Raman spectroscopy. Spectrochim. Acta, Part A 59, 2267–2276. https://doi.org/10.1016/S1386-1425(03)00070-2.

Brandon, K.A., Roden-Tice, T.M., Garver, J.I., 1998. Late Caneozoic exhumation of the Cascadia accretionnary wedge in the Olympic montains, Northwest Washington State. Geol. Soc. Am. Bull. 110, 985–1009. https://doi.org/10.1130/0016-7606(1998)110<0985:LCEOTC>2.3.CO;2.

Buseck, P.R., Huang, B.J., 1985. Conversion of carbonaceous material to graphite during Metamorphism. Geochim. Cosmochim. Acta 49, 2003–2016. https://doi.org/10.1016/00167037(85)90059-6.

Calle, A.Z., Horton, B.K., Garcia-Duarte, R., Flaig, P.P., 2017. Neoproterozoic-Paleozoic Tectonics and Paleogeography of the west-central South America convergent margin from detrital zircon geochronology. Geol. Soc. Am. Abstr. Programs 49. https://doi.org/10.1130/abs/2017AM-305408.

Carrapa, B., DeCelles, P.G., Reiners, P.W., Gehrels, G.E., Masafumi, S., 2009. Apatite triple dating and white mica 40Ar/39Ar thermochronology of syntectonic detritus in the Central Andes: a multiphase tectonothermal history. Geology 37, 407–410. https://doi.org/10.1130/G25698A.1.

Cawood, P.A., 2005. Terra Australis Orogen: Rodinia breakup and development of the Pacific and Iapetus margins of Gondwana during the Neoproterozoic and Paleozoic. Earth Sci. Rev. 69, 249–279.

Cawood, P.A., Buchan, C., 2007. Linking accretionary orogenesis with supercontinent assembly. Earth-Sci. Rev. 82, 217–256.

Cawood, P.A., Kröner, A., Collins, W., Kusky, T.M., Mooney, W.D., Windley, B.F., 2009. Accretionary orogens through Earth history. Geol. Soc. Lond., Spec. Publ. 318, 1–36. https://doi.org/10.1144/SP318.1.

Harrison, T.M., Célérier, J., Aikman, A.B., Hermann, J., Heizler, M.T., 2009. Diffusion of ^{40}Ar in muscovite. Geochim. Cosmochim. Acta 73, 1039–1051.

Clauer, N., 2013. The K-Ar and ^{40}Ar/^{39}Ar methods revisited for dating fine-grained K-bearing clay Minerals. Chem. Geol. 354, 163–185.

Coira, B., Davidson, J., Mpodozis, C., Ramos, V., 1982. Tectonic and magmatic evolution of the Andes of northern Argentina and Chile. In: Linares (Ed.), A Symposium on the Magmatic Evolution of the Andes. 18. Earth-Sciences Review, pp. 303–332. https://doi.org/10.1016/j.chemgeo.2013.05.030.

Coira, B., Pérez, B., Flores, P., Kay, S.M., Woll, B., Hanning, M., 1999. Magmatic sources and tectonic setting of Gondwanan margin Ordovician magmas, northern Puna of Argentina and Chile. In: Ramos, V.A., Keppie, J.D. (Eds.), Laurentia-Gondwana Connections before Pangea. Geological Society of America Special Paper vol. 336, pp. 145–170.

Coney, P.J., Evenchick, C.A., 1994. Consolidation of the American Cordilleras. J. S. Am. Earth Sci. 7, 241–262. https://doi.org/10.1016/0895-9811(94)90011-6.

Cooper, F.J., Hodges, K.V., Adams, B.A., 2013. Metamorphic constraints on the character and displacement of the south Tibetan fault system, central Bhutanese Himalaya. Lithosphere 5, 67–81. https://doi.org/10.1130/L221.1.

Cottle, J.M., Waters, D.J., Riley, D., Beyssac, O., Jessup, M.J., 2011. Metamorphic history of the South Tibetan Detachment System, Mt. Everest region, revealed by the RSCM thermometry and phase equilibria modelling. J. Metamorph. Geol. 29, 561–582. https://doi.org/10.1111/j.1525-1314.2011.00930.x.

van Daalen, M., Heilbronner, R., Kunze, K., 1999. Orientation analysis of localized shear deformation in quartz fibres at the brittle-ductile transition. Tectonophysics 303, 83–107.

DeCelles, P.G., Giles, K.N., 1996. Foreland basin systems. Basin Res. 8, 105–123.

DeCelles, P.G., Horton, B.K., 2003. Early to middle Tertiary foreland basin development and the history of Andean crustal shortening in Bolivia. Geol. Soc. Am. Bull. 115, 58–77. https://doi.org/10.1130/0016-7606(2003)115<0058:ETMTFB>2.0.CO;2.

DeCelles, P.G., Mitra, G., 1995. History of the Sevier orogenic wedge in terms of critical taper models, northeast Utah and southwest Wyoming. Geol. Soc. Am. Bull. 107, 454–462. https://doi.org/10.1130/0016-7606(1995)107<0454:HOTSOW>2.3.CO;2.

Domeier, M., Torsvik, T.H., 2014. Plate tectonics in the late Paleozoic. Geosci. Front. 5, 303–350. https://doi.org/10.1016/j.gsf.2014.01.002.

Drury, M.R., Urai, J.L., 1990. Deformation-related recrystallization processes. Tectonophysics 172, 235–253.

Drury, M.R., Humphreys, F.J., White, S.H., 1985. Large strain deformation studies using polycrystalline magnesium as a rock analogue. Part II: dynamic recrystallisation mechanisms at high temperatures. Phys. Earth Planet. Inter. 40, 208–222.

Dunlap, W.J., Hirth, G., Teyssier, C., 1997. Thermomechanical evolution of a ductile duplex. Tectonics 16, 983–1000.

Dunn, J., Hartshorn, K., Hartshorn, P., 1995. Structural styles and hydrocarbon potential of the sub-Andean thrust belt of southern Bolivia. In: Tankard, A.J., et al. (Eds.), Petroleum Basins of South America. 62. American Association of Petroleum Geologists Memoir, pp. 523–543.

Egenhoff, S.O., 2007. Life and death of a Cambrian–Ordovician basin: an Andean three-act play featuring Gondwana and the Arequipa-Antofalla terrane. In: Linnemann, U., et al. (Eds.), The Evolution of the Rheic Ocean: From Avalonian-Cadomian Active Margin to Alleghenian- Variscan Collision. 423. Geological Society of America Special Paper, pp. 511–524. https://doi.org/10.1130/2007.2423(26).

Egenhoff, S.O., Maletz, J., Weber, B., Erdtmann, B.-D., 2002. The middle Ordovician Jurcuma section: a pinpoint for the evolution of southern Bolivia. Freib. Forsch. C497, 9–17.

Egenhoff, S.O., Maletz, J., Erdtmann, B.-D., 2004. Lower Ordovician graptolite biozonation and lithofacies of southern Bolivia: relevance for palaeogeographic interpretations. Geol. Mag. 141, 287–299.

Eichelberger, N., McQuarrie, N., 2015. Kinematic reconstruction of the Bolivian orocline. Geosphere 11, 445–462. https://doi.org/10.1130/GES01064.1.

Eichelberger, N., McQuarrie, N., Ehlers, T.A., Enkelmann, E., Barnes, J.B., Lease, R.O., 2013. New constraints on the chronology, magnitude, and distribution of deformation within the central Andean orocline. Tectonics 32, 1432–1453. https://doi.org/10.1002/tect.20073.

Einhorn, J.C., Gehrels, G.E., Vernon, A., Decelles, P.G., 2015. U-Pb zircon geochronology of Neoproterozoic – Paleozoic sandstones and Paleozoic plutonic rocks in the Central Andes (21°S – 26°S). In: DeCelles, P.G., Ducea, M.N., Carrapa, B., Kapp, P.A. (Eds.), Geodynamics of a Cordilleran Orogenic System: The Central Andes of Argentina and Northern Chile. Geological Society of America Memoir vol. 212, pp. 115–124. https://doi.org/10.1130/2015.1212(06.

Elger, K., Oncken, O., Glodny, J., 2005. Plateau-style accumulation of deformation: Southern Altiplano. Tectonics 24, TC4020. https://doi.org/10.1029/2004TC001675.

Espurt, N., Brusset, S., Baby, P., Hermoza, W., Bolaños, R., Uyen, D., Déramond, J., 2008. Paleozoic structural controls on shortening transfer in the Subandean foreland thrust system, Ene and southern Ucayali basins, Peru. Tectonics 27, TC3009. https://doi.org/10.1029/2007TC002238.

Giambiagi, L., Mescua, J., Bechis, F., Martinez, A., Folguera, A., 2011. Pre-Andean deformation of the Precordillera southern sector, southern Central Andes. Geosphere 7, 219–239. https://doi.org/10.1130/GES00572.1.

Giraudo, R., Limachi, R., 2001. Pre-Silurian control in the genesis of the central and southern Bolivian foldbelt. J. S. Am. Earth Sci. 14, 665–680. https://doi.org/10.1016/S0895-9811(01)00068-2.

Gleadow, A.J.W., Duddy, I.R., Green, P.F., Lovering, J.F., 1986. Confined fission track lengths in apatite: a diagnostic tool for thermal history analysis. Contrib. Mineral. Petrol. 94, 405–415.

Gohrbandt, K.H.A., 1993. Paleozoic paleogeographic and depositional developments on the central proto-Pacific margin of Gondwana: their importance to hydrocarbon accumulation. J. S. Am. Earth Sci. 6, 267–287.

Götze, H.J., Lahmeyer, B., Schmidt, S., Strunk, S., 1994. The lithospheric structure of the Central Andes (20–25°S) as inferred from quantitative interpretation of regional gravity. In: Reutter, K.J., et al. (Eds.), Tectonics of the Southern Central Andes. Springer, Berlin, pp. 7–22.

Gubbels, T., Isacks, B., Farrar, E., 1993. High-level surfaces, plateau uplift, and foreland development, Bolivian Central Andes. Geology 21, 695–698.

Guenthner, W.R., Reiners, P.W., Ketcham, R.A., Nasdala, L., Giester, G., 2013. Helium diffusion in natural zircon: radiation damage, anisotropy, and the interpretation of zircon (U-Th)/He thermochronology. Am. J. Sci. 313, 145–198. https://doi.org/10.2475/03.2013.01.

Haines, S.H., van der Pluijm, B.A., 2008. Clay quantification and Ar – Ar dating of synthetic and natural gouge: application to the Miocene Sierra Mazatán detachment fault, Sonora, Mexico. J. Struct. Geol. 30, 525–538. https://doi.org/10.1016/j.jsg.2007.11.012.

Hérail, G., Oller, J., Baby, P., Bonhomme, M., Soler, P., 1996. Strike-slip faulting, thrusting and related basins in the Cenozoic evolution of the southern branch of the Bolivian

orocline. Tectonophysics 259, 201–212. https://doi.org/10.1016/0040-1951(95)00108-5.

Heredia, N., et al., 2018. Review of the geodynamic evolution of the SW margin of Gondwana preserved in the Central Andes of Argentina and Chile (28°-38° S latitude). J. S. Am. Earth Sci. 87, 87–94.

Horton, B., 2000. Sediment accumulation on top of the Andean orogenic wedge: oligocene to late Miocene basins of the Eastern Cordillera, southern Bolivia. Reply. Geol. Soc. Am. Bull. 112, 1756–1759. https://doi.org/10.1130/0016-7606(2000)112<1756:R>2.0.CO;2.

Horton, B.K., 1998. Sediment accumulation on top of the Andean orogenic wedge: Oligocene to late Miocene basins of the Eastern Cordillera, southern Bolivia. Geol. Soc. Am. Bull. 110, 1174–1192. https://doi.org/10.1130/00167606(1998)110<1174:SAOTOT>2.3.CO;2.

Horton, B.K., 2005. Revised deformation history of the Central Andes: Inferences from Cenozoic foredeep and intermontane basins of the Eastern Cordillera, Bolivia. Tectonics 24, TC3011. https://doi.org/10.1029/2003TC001619.

Horton, B.K., 2018a. Tectonic regimes of the central and southern Andes: responses to variations in plate coupling during subduction. Tectonics 37, 402–429. https://doi.org/10.1002/2017TC004624.

Horton, B.K., 2018b. Sedimentary record of Andean mountain building. Earth Sci. Rev. 178, 279–309. https://doi.org/10.1016/j.earscirev.2017.11.025.

Horton, B.K., Hampton, B.A., Wanders, G.L., 2001. Paleogene synorogenic sedimentation in the Altiplano plateau and implications for initial mountain building in the central Andes. Geol. Soc. Am. Bull. 113, 1387–1400. https://doi.org/10.1130/0016-7606(2001)113<1387:PSSITA>2.0.CO;2.

Hunziker, J.C., Frey, M., Clauer, N., Dallmeyer, R.D., Friedrichsen, H., Flehmig, W., Hochstrasser, K., Roggwiler, P., Schwander, H., 1986. The evolution of illite to muscovite, mineralogical and isotopic data from the Glarus Alps, Switzerland. Contrib. Mineral. Petrol. 92, 157–180.

Isaacson, P.E., 1975. Evidence for a western extracontinental land source during the Devonian Period in the Central Andes. Geol. Soc. Am. Bull. 86, 39–46.

Isaacson, P.E., Díaz Martínez, E., 1995. Evidence for a middle–late Paleozoic foreland basin and significant paleolatitudinal shift, Central Andes. In: Tankard, A.J., Suárez Soruco, R., Welsink, H.J. (Eds.), Petroleum Basins of South America. 62. American Association of Petroleum Geologists Memoir, pp. 231–249.

Isaacson, P.E., Palmer, B.A., Mamet, B.L., Cooke, J.C., Sanders, D.E., 1995. Devonian–Carboniferous Stratigraphy in the Madre de Dios Basin, Bolivia: Pando X-1 and Manuripi X-1 Wells. In: Tankard, A.J., Suárez Soruco, R., Welsink, H.J. (Eds.), Petroleum Basins of South America. 62. American Association of Petroleum Geologists Memoir, pp. 501–510.

Isacks, B., 1988. Uplift of the central Andean plateau and bending of the Bolivian orocline. J. Geophys. Res. 93, 3211–3231. https://doi.org/10.1029/JB093iB04p03211.

Jaboyedoff, M., Cosca, M.A., 1999. Dating incipient metamorphism using $^{40}Ar/^{39}Ar$ geochronology and XRD modeling: a case study from the Swiss Alps. Contrib. Mineral. Petrol. 135, 93–113.

Jacobshagen, V., Müller, J., Wemmer, K., Ahrendt, H., Manutsoglu, E., 2002. Hercynian deformation and metamorphism in the Cordillera oriental of Southern Bolivia, Central Andes. Tectonophysics 345, 119–130.

Ji, J., Browne, P.R.L., 2000. Relationship between illite crystallinity and temperature in active geothermal systems of New Zealand. Clays Clay Min. 48, 139–144.

Kennan, L., Lamb, S., Hoke, L., 1997. High-altitude paleosurfaces in the Bolivian Andes: Evidence for late Cenozoic surface uplift. In: Widdowson, M. (Ed.), Paleosurfaces: Recognition, Reconstruction and Paleoenvironmental Interpretation. Geological Society, London, pp. 307–323 Special Publication 120.

Ketcham, R.A., 2005. Forward and inverse modeling of low-temperature thermochronometry data. Rev. Mineral. Geochem. 58, 275–314. https://doi.org/10.2138/rmg.2005.58.11.

Kleiman, L., Japas, M., 2009. The Choiyoi volcanic province at 34°S-36°S (San Rafael, Mendoza, Argentina): Implications for the late Palaeozoic evolution of the southwestern margin of Gondwana. Tectonophysics 473 (3), 283–289. https://doi.org/10.1016/j.tecto.2009.02.046.

Kley, J., 1996. Transition from basement-involved to thin-skinned thrusting in the Cordillera oriental of southern Bolivia. Tectonics 15, 763–775. https://doi.org/10.1029/95TC03868.

Kley, J., Reinhardt, M., 1994. Geothermal and tectonic evolution of the Eastern Cordillera and the Subandean Ranges of Southern Bolivia. In: Reutter, K.J., Scheuber, E., Wigger, P. (Eds.), Tectonics of the Southern Central Andes. Springer-Verlag, Berlin, pp. 155–170.

Kley, J., Gangui, A.H., Kruger, D., 1996. Basement-involved blind thrusting in the eastern Cordillera oriental, southern Bolivia: evidence from cross sectional balancing, gravimetric and magnetotelluric data. Tectonophysics 259, 171–184. https://doi.org/10.1016/0040-1951(95)00067-4.

Kley, J., Muller, J., Tawackoli, S., Jacobshagen, V., Manutsoglu, E., 1997. Pre-Andean and Andean-age deformation in the Eastern Cordillera of southern Bolivia. J. S. Am. Earth Sci. 10, 1–19. https://doi.org/10.1016/S0895-9811 (97)00001-1.

Kley, J., Monaldi, C.R., Salfity, J.A., 1999. Along-strike segmentation of the Andean foreland: causes and consequences. Tectonophysics 301, 75–94. https://doi.org/10.1016/S0040-1951(98)90223-2.

Koltonik, K., Isaacson, P.E., Pisarzowska, A., Paszkowski, M., Augustsson, C., Szczerba, M., Slama, J., Budzyn, B., Stachacz, M., Krawczynski, W., 2019. Provenance of upper Paleozoic siliciclastics rocks from two high-latitude glacially influenced intervals in Bolivia. J. S. Am. Earth Sci. 92, 12–31.

Kübler, B., 1967. La cristallinite´ de l'illite et les zones tout a'fait supe'rieures du me'tamorphisme, in Etages Tectoniques, Colloque de Neucha^tel 1966. Universite´ Neucha^tel, a` la Baconnie're, Neucha^tel, Switzerland.

Kübler, B., Jaboyedoff, M., 2000. Illite crystallinity. Comptes Rendus de l'Acade'mie des. Sciences 331, 75–89.

Law, R.D., 2014. Deformation thermometry based on quartz c-axis fabrics and recrystallization microstructures: a review. J. Struct. Geol. 66, 129–161. https://doi.org/10.1016/j.jsg.2014.05.023.

Law, R.D., Stahr, D.W., Francsis, M.K., Ashley, K.T., Grasemann, B., Ahmad, T., 2013. Deformation temperatures and flow vorticities near the base of the Greater Himalayan Series, Sutlej Valley and Shimla Klippe, NW India. J. Struct. Geol. 54, 21–53. https://doi.org/10.1016/j.jsg.2013.05.009.

Long, S.P., Soignard, E., 2016. Shallow-crustal metamorphism during late cretaceous anatexis in the Sevier hinterland plateau: peak temperature conditions from the Grant Range, eastern Nevada, U.S.a. Lithosphere 8, 150–164. https://doi.org/10.1130/L501.1.

Long, S.P., Gordon, S.M., Young, J.P., Soignard, E., 2016. Temperature and strain gradients through Lesser Himalayan rocks and across the Main Central thrust, south-Central Bhutan: Implications for transport-parallel stretching and inverted metamorphism. Tectonics 35, 1863–1891. https://doi.org/10.1002/2016TC004242.

Long, S.P., Gordon, S.M., Soignard, E., 2017. Distributed north-vergent shear and flattening through Greater and Tethyan Himalayan rocks: insights from metamorphic and strain data from the Dang Chu region, Central Bhutan. Lithosphere 9, 774–795. https://doi.org/10.1130/L655.1 1.

Lucassen, F., Lewerenz, S., Franz, G., Viramonte, J., Mezger, K., 1999. Metamorphism, isotopic ages and composition of lower crustal granulite xenoliths from the cretaceous Salta Rift, Argentina. Contrib. Mineral. Petrol. 134, 325–341. https://doi.org/10.1007/s004100050488.

Maletz, J., Egenhoff, S.O., 2001. Late Tremadoc to early Arenig graptolite faunas of southern Bolivia and their implications for a worldwide biozonation. Lethaia 34, 47–62.

Maloney, K.T., Clarke, G.L., Klepeis, K.A., Quevedo, L., 2013. The late Jurassic to present evolution of the Andean margin: drivers and the geological record. Tectonics 32, 1049–1065. https://doi.org/10.1002/tect.20067.

Manutsoglu, E., Müller, J., Mertmann, D., Jacobshagen, V., 1998. Thermal influences on Paleozoic sediments based on illite– crystallinity data (Section Tarija–San Vicente, Eastern Cordillera, southern Bolivia). Terra Nostra 98/5 (16), 107 LAK Bayreuth.

Martinod, J., Gérault, M., Husson, L., Regard, V., 2020. Widening of the Andes: an interplay between subduction dynamics and crustal wedge tectonics. Earth-Sci. Rev. 204, 103170. https://doi.org/10.1016/j.earscirev.2020.103170.

Matthews, K.J., Maloney, K.T., Zahirovic, S., Williams, S.E., Seton, M., Müller, R.D., 2016. Global plate boundary evolution and kinematics since the late Paleozoic. Glob. Planet. Chang. 146, 226–250. https://doi.org/10.1016/j.gloplacha.2016.10.002.

McGroder, M.F., Lease, R.O., Pearson, D.M., 2015. Along-strike variation in structural styles and hydrocarbon occurrences, Subandean fold-and-thrust belt and inner foreland, Colombia to Argentina. In: DeCelles, P.G., Ducea, M.N., Carrapa, B., Kapp, P.A. (Eds.), Geodynamics of a Cordilleran Orogenic System: The Central Andes of Argentina and Northern Chile. 212. Geological Society of America Memoir, pp. 79–113. https://doi.org/10.1130/2015.1212(05).

McQuarrie, N., 2002. The kinematic history of the central Andean fold-thrust belt, Bolivia: Implications for building a high plateau. Geol. Soc. Am. Bull. 114, 950–963. https://doi.org/10.1130/0016-7606(2002)114<0950.

McQuarrie, N., DeCelles, P., 2001. Geometry and structural evolution of the central Andean backthrust belt, Bolivia. 20. Tectonics, pp. 669–692. https://doi.org/10.1029/2000TC001232.

Merriman, R.J., Frey, M., 1999. Pattern of very low-grade metamorphism in metapelitic rocks. In: Frey, M., Robinson, D. (Eds.), Low- Grade Metamorphism. Blackwell Science, Oxford, pp. 61–107.

Merriman, R.J., Peacor, D.R., 1999. Very low-grade metapelites: Mineralogy, microfabrics and measuring reaction progress. In: Frey, M., Robinson, D. (Eds.), Low-Grade Metamorphism. Blackwell Science, Oxford, pp. 10–60.

Mon, R., Hongn, F., 1991. The structure of the Precambrian and lower Paleozoic basement of the Central Andes between 22° and 32° S Lat. Geol. Rundsch. 80, 745–758. https://doi.org/10.1007/BF01803699.

Mon, R., Salfity, J.A., 1995. Tectonic evolution of the Andes of Northern Argentina. In: Tankard, A.J., Suárez Soruco, R., Welsink, H.J. (Eds.), Petroleum Basins of South America. 62. American Association of Petroleum Geologists Memoir, pp. 269–284.

Moore, D.M., Reynolds Jr., R.C., 1997. X-Ray Diffraction and the Identification and Analysis of Clay Minerals. Oxford University Press, Oxford.

Mpodozis, C., Ramos, V.A., 1989. The Andes of Chile and Argentina. In: Ericksen, G.E., Cañas Pinochet, M.T., Reinemund, J.A. (Eds.), Geology of the Andes and its Relation to Hydrocarbon and Mineral Resources. Houston, Texas, Circum-Pacific Council for Energy and Mineral Resources, pp. 59–90.

Mukhopadhyay, P., 1994. Vitrinite reflectance as a maturity parameter: Petrographic and molecular characterization and its application to basin modeling. In: Mukhopadhyay, P., Dow, W.G. (Eds.), Vitrinite Reflectance as a Maturity Parameter: Applications and Limitations. vol. 570. American Chemical Society, Symposium Series, Washington D.C., pp. 1–24.

Müller, J.P., Kley, J., Jacobshagen, V., 2002. Structure and Cenozoic kinematics of the Eastern Cordillera, southern Bolivia (21°S). Tectonics 21, 1037. https://doi.org/10.1029/2001TC001340.

Nance, R.D., Gutiérrez-Alonso, G., Keppie, J.D., Linnemann, U., Murphy, J.B., Quesada, C., Strachan, R.A., Woodcock, N.H., 2010. Evolution of the Rheic Ocean. Gondwana Res. 17, 194–222.

Hunter, Nicholas J.R., Weinberg, Roberto F., Wilson, Christopher J.L., Santanu Misra, Vladimir Luzin, 2018. Microscopic anatomy of a "hot-on-cold" shear zone: Insights from quartzites of the Main Central Thrust in the Alaknanda region (Garhwal Himalaya). GSA Bulletin 130 (9-10), 1519–1539. https://doi.org/10.1130/B31797.

Oriolo, S., Schulz, B., González, P.D., Bechis, F., Olaizola, E., Krause, J., Renda, E.M., Vizán, H., 2019. The late Paleozoic tectonometamorphic evolution of patagonia revisited:

insights from the pressure-temperature-deformation-time (P-T-D-t) path of the Gondwanide basement of the North Patagonian Cordillera (Argentina). Tectonics 38, 2378–2400. https://doi.org/10.1029/2018TC005358.

Pearson, D.M., Kapp, P., Reiners, P.W., Gehrels, G.E., Ducea, M.N., Pullen, A., Otamendi, J.E., Alonso, R.N., 2012. Major Miocene exhumation by fault-propagation folding within a metamorphosed, early Paleozoic thrust belt: Northwestern Argentina. Tectonics 31, TC4023. https://doi.org/10.1029/2011TC003043.

Rahl, J.M., Anderson, K.M., Brandon, M.T., Fassoulas, C., 2005. Raman spectroscopic carbonaceous material thermometry of low-grade metamorphic rocks: calibration and application to tectonic exhumation in Crete, Greece. Earth Planet. Sci. Lett. 240, 339–354. https://doi.org/10.1016/j.epsl.2005.09.055.

Rahl, J.M., Haines, S.H., van der Pluijm, B.A., 2011. Links between orogenic wedge deformation and erosional exhumation: evidence from illite age analysis of fault rock and detrital thermochronology of syn-tectonic conglomerates ion the Spanish Pyrenees. Earth Planet. Sci. Lett. 307, 180–190.

Ramos, V.A., 2008. The basement of the Central Andes: the Arequipa and related terranes. Annu. Rev. Earth Planet. Sci. 36, 289–324. https://doi.org/10.1146/annurev.earth.36.031207.124304.

Ramos, V.A., 2009. Anatomy and global context of the Andes: Main geologic features and the Andean orogenic cycle. In: Kay, S.M., Ramos, V.A., Dickinson, W.R. (Eds.), Backbone of the Americas: Shallow Subduction, Plateau Uplift, and Ridge and Terrane Collision. vol. 204. Geological Society of America Memoir, pp. 31–65. https://doi.org/10.1130/2009.1204(02).

Ramos, V.A., 2018. The Famatinian Orogen along the Protomargin of Western Gondwana: evidence for a nearly Continuous Ordovician Magmatic Arc between Venezuela and Argentina. In: Folguera, et al. (Eds.), The evolution of the Chilean-Argentinian Andes. Springer Earth System Sciences, pp. 154–183.

Ramos, V.A., Aleman, A., 2000. Tectonic evolution ofthe Andes. In: Cordani, U.G., Milani, E.J., Thomaz Filha, A., Campos, D.A. (Eds.), Tectonic Evolution of South America. 31st International Geological Congress, Rio de Janerio, pp. 635–685.

Rapela, C.W., Pankhurst, R.J., Casquet, C., Dahlquist, J.A., Fanning, C.M., Baldo, E.G., Galindo, C., Alasino, P.H., Ramacciotti, C.D., Verdecchia, S.O., Murra, J.A., Basei, M.A., 2018. A review of the Famatinian Ordovician magmatism in southern South America: evidence of lithosphere reworking and continental subduction in the early proto-Andean margin of Gondwana. Earth Sci. Rev. 187, 259–285. https://doi.org/10.1016/j.earscirev.2018.10.006.

Reiners, P.W., Spell, T.L., Nicolescu, S., Zanetti, K.A., 2004. Zircon (U-Th)/he thermochronometry: he diffusion and comparisons with $^{40}Ar/^{39}Ar$ dating. Geochim. Cosmochim. Acta 68, 1857–1887. https://doi.org/10.1016/j.gca.2003.10.021.

Reiners, P.W., Ehlers, T.a., Zeitler, P.K., 2005. Past, present, and future of thermochronology. Rev. Mineral. Geochem. 58, 1–18. https://doi.org/10.2138/rmg.2005.58.1.

Salfity, J.A., Marquillas, R.A., 1994. Tectonic and sedimentary evolution of the Cretaceous–Eocene Salta Group basin, Argentina. In: Salfity, J.A. (Ed.), Cretaceous Tectonics of the Andes: Wiesbaden. Vieweg Publishing, Germany, pp. 266–315.

Sempere, T., 1995. Phanerozoic evolution of Bolivia and adjacent regions. In: Tankard, A.J., Suárez Soruco, R., Welsink, H.J. (Eds.), Petroleum Basins of South America. 62. American Association of Petroleum Geologists Memoir, pp. 207–230.

Sempere, T., 2000. Sediment accumulation on top of the Andean orogenic wedge: oligocene to late Miocene basins of the Eastern Cordillera, southern Bolivia. Discussion and Reply. Geol. Soc. Am. Bull. 112, 1752–1755. https://doi.org/10.1130/0016-7606(2000)112<1752:DSAOTO>2.0.CO;2.

Sempere, T., Butler, R.F., Richards, D.R., Marshall, L.G., Sharp, W., Swisher III, C.C., 1997. Stratigraphy and chronology of Upper Cretaceous–lower Paleogene strata in Bolivia and northwest Argentina. Geol. Soc. Am. Bull. 109, 709–727. https://doi.org/10.1130/0016-7606(1997)109<0709:SACOUC>2.3.CO;2.

Sempere, T., et al., 2002. Late Permian–Middle Jurassic lithospheric thinning in Peru and Bolivia, and its bearing on Andean-age tectonics. Tectonophysics 345, 153–181. https://doi.org/10.1016/S0040-1951(01)00211-6.

Servicio Geologico de Bolivia, 1992. Mapas Tematicos de Recursos Minerales de Bolivia, Hojas Tarija y Villazon. Servicio Geologico de Bolivia serie II-MTB-1B, scale 1:250,000.

Servicio Nacional de Geología y Técnico de Minas, 2010. Carta Geologica de Bolivia, Hoja 6329 Chilcobija. Servicio Nacional de Geología y Técnico de Minas SGTM serie I–CGB-57, scale 1:100,000.

Starck, D., 1995. Silurian–Jurassic stratigraphy and basin evolution of north- western Argentina. In: Tankard, A.J., Suárez Soruco, R., Welsink, H.J. (Eds.), Petroleum Basins of South America. 62. American Association of Petroleum Geologists Memoir, pp. 251–267.

Starnes, J.K., Long, S.P., Gordon, S.M., Zhang, J., Soignard, E., 2020. Using quartz fabric intensity parameters to delineate strain patterns across the Himalayan Main Central thrust. J. Struct. Geol. 131 (103941), 18. https://doi.org/10.1016/j.jsg.2019.103941.

Stipp, M., Stunitz, H., Heilbronner, R., Schmid, S.M., 2002. The eastern Tonale fault zone: a 'natural laboratory' for crystal plastic deformation over a temperature range from 250° to 700°C. J. Struct. Geol. 24, 1861–1884. https://doi.org/10.1016/S0191-8141(02)00035-4.

Stockli, D.F., 2005. Application of low-temperature thermochronometry to extensional tectonic settings. Rev. Mineral. Geochem. 58, 411–448. https://doi.org/10.2138/rmg.2005.58.16.

Süssenberger, A., Wemmer, K., Schmidt, S.T., 2018. The zone of incipient 40 Ar* loss-monitoring Ar * degassing behavior in a contact metamorphic setting. Appl. Clay Sci. 165, 52–63. https://doi.org/10.1016/j.clay.2018.07.040.

Tankard, A.J., Uliana, M.A., Welsink, H.J., Ramos, V.A., Turic, M., França, A.B., Milani, E.J., de Brito Neves, B., Eyles, N., Skarmeta, J., Santa Ana, H., Wiens, F., Cirbián, M., López, P.O., De Wit, G.J.B., Machacha, T., Miller, R.McG, 1995. Tectonic controls of basin evolution in southwestern Gondwana. In: Tankard, A.J., Suárez Soruco, R., Welsink, H.J. (Eds.), Petroleum Basins of South America. 62. American Association of Petroleum Geologists Memoir, pp. 5–52.

Tröeng, B., Claure, H., Oliveira, L., Baelon, R., Walser, G., 1993. Mapas temáticos de recursos minerales de Bolivia: Hojas Tarija y Villazón. Bol. Serv. Geol. Boli. 3.

Troth, I., Marshall, J.E.A., Racey, A., Becker, R.T., 2010. Devonian Sea-Level Change in Bolivia: a high palaeolatitude biostratigraphical calibration of the global sea-level curve. Palaeogeogr. Palaeoclimatol. Palaeoecol. https://doi.org/10.1016/j.palaeo.2010.10.008.

Uba, C.E., Heubeck, C., Hulka, C., 2006. Evolution of the late Cenozoic Chaco foreland basin, southern Bolivia. Basin Res. 18, 145–170. https://doi.org/10.1111/j.1365-2117.2006.00291.x.

Verdel, C., Niemi, N., van der Pluijm, B.A., 2011. Variations in the illite-muscovite transition related to metamorphic conditions and detrital muscovite content: insight from the Paleozoic passive margin of the S.W. US. J. Geol. 119, 419–437. https://doi.org/10.1086/660086.

Verdel, C., van der Pluijm, B.A., Niemi, N., 2012. Variation of illite/muscovite $^{40}Ar/^{39}Ar$ age spectra during progressive low-grade metamorphism: an example from the US Cordillera. Contrib. Mineral. Petrol. 164, 521–536. https://doi.org/10.1007/s00410-012-0751-7.

Weinberg, R.F., Becchio, R., Farias, P., Suzaño, N., Sola, A., 2018. Early Paleozoic accretionary orogenies in NW Argentina: growth of West Gondwana. Earth Sci. Rev. 187, 219–247.

Welsink, H.J., Franco, M., Oviedo, G.C., 1995a. Andean and Pre-Andean deformation, Boomerang Hills Area, Bolivia. In: Tankard, A.J., Suárez Soruco, R., Welsink, H.J. (Eds.), Petroleum Basins of South America. 62. American Association of Petroleum Geologists Memoir, pp. 481–499.

Welsink, H.J., Martinez, E., Aranibar, O., Jarandilla, J., 1995b. Structural inversion of a cretaceous rift basin, Southern Altiplano, Bolivia. In: Tankard, A.J., Suárez Soruco, R., Welsink, H.J. (Eds.), Petroleum Basins of South America. 62. American Association of Petroleum Geologists Memoir, pp. 305–324.

Wigger, P., et al., 1994. Variation in the crustal structure of the southern Central Andes deduced from seismic refraction investigations. In: Reutter, L., et al. (Eds.), Tectonics of the Southern Central Andes. Springer-Verlag, New York, pp. 23–48 https://doi.org/10.1007/978-3-642-77353-2_2.

Wyld, S.J., Rogers, J.W., Copeland, P., 2003. Metamorphic evolution of the Luning-Fencemaker fold-thrust belt, Nevada: Illite crystallinity, metamorphic petrology, and $^{40}Ar/^{39}Ar$ geochronology. J. Geol. 111, 17–38.

Yamada, R., Murakami, M., Tagami, T., 2007. Statistical modelling of annealing kinetics of fission tracks in zircon: Reassessment of laboratory experiments. Chem. Geol. 236, 75–91. https://doi.org/10.1016/j.chemgeo.2006.09.002.

Zhu, C., Song, R., Shengbiao, H., 2016. Application of illite crystallinity for paleo- temperature reconstruction: a case study in the western Sichuan Basin, SW China. Carpath. J. Earth Environ. Sci. 11, 599–608.